

Hippocampal neuronal activity is aligned with action plans

<https://doi.org/10.1038/s41586-024-08397-7>

Received: 16 February 2024

Accepted: 31 October 2024

Published online: 08 January 2025

 Check for updates

Ipsita Zutshi¹, Athina Apostolelli¹, Wannan Yang^{1,2}, Zheyang Sam Zheng^{1,2}, Tora Dohi¹, Edoardo Balzani^{2,3}, Alex H. Williams^{2,4}, Cristina Savin^{2,3} & György Buzsáki¹✉

Neurons in the hippocampus are correlated with different variables, including space, time, sensory cues, rewards and actions, in which the extent of tuning depends on ongoing task demands^{1–8}. However, it remains uncertain whether such diverse tuning corresponds to distinct functions within the hippocampal network or whether a more generic computation can account for these observations⁹. Here, to disentangle the contribution of externally driven cues versus internal computation, we developed a task in mice in which space, auditory tones, rewards and context were juxtaposed with changing relevance. High-density electrophysiological recordings revealed that neurons were tuned to each of these modalities. By comparing movement paths and action sequences, we observed that external variables had limited direct influence on hippocampal firing. Instead, spiking was influenced by online action plans and modulated by goal uncertainty. Our results suggest that internally generated cell assembly sequences are selected and updated by action plans towards deliberate goals. The apparent tuning of hippocampal neuronal spiking to different sensory modalities might emerge due to alignment to the afforded action progression within a task rather than representation of external cues.

The hippocampus is often portrayed as a structure at the top of the cortical hierarchy, which receives highly processed sensory modalities. It is assumed to synthesize those modalities into abstract space and time, explicitly reflected by the place and time fields of its neurons¹⁰. Other considerations suggest that it is part of a top-down effector system involved in planning and initiating voluntary actions^{11,12}. In collaboration with frontal cortical areas^{13,14}, it can also sustain working memory, possibly related to the preparation for upcoming actions¹⁵. Combining the sensory synthesis and effector systems supports effective navigation in an environment¹⁶ in the form of a predictive code¹⁷. By disengaging from the environment, the hippocampus can support memory and planning¹⁸.

Of these views, spatial navigation and sensory synthesis have received most attention^{19,20}. Yet, whether one framework can satisfactorily incorporate competing views and explain experimental data has remained a challenge⁹. A critical problem is that the experimental design strongly influences the findings and their interpretation. By designing experiments in which space, time, action, memory or sensory modality is the relevant domain, one finds a description of place fields, time fields, reward cells, speed cells, tone cells, choice cells or ‘engram’ cells in the hippocampus^{1–8}. The implicit assumption is that each label reflects unique computations performed by the hippocampus, generating ‘representations’ specific to the relevant modality and reflecting different functions of hippocampal firing. Yet, a common confound is that the behaviour of animals becomes inevitably linked to the relevant domain¹¹.

To disentangle task-specific sensory variables, motor actions and intentions, we designed a task that incorporated multiple behaviourally

relevant domains and controls. By comparing similar movement trajectories and actions across task contingencies, we tested whether the firing of hippocampal neurons was driven by a general internal computation applied across all monitored modalities.

Mouse-controlled auditory navigation task

We implemented an agent-controlled auditory navigation task to disambiguate tuning to spatial coordinates versus auditory tones (Fig. 1a, Extended Data Fig. 1a and Supplementary Videos 1 and 2). Mice ($n = 6$) ran on a linear track with 7 equally spaced water ports. During no-tone trials, they ran back and forth to collect water rewards at either end with no auditory tones playing. During tone trials, a tone ascended in frequency (2–25 kHz) in a closed-loop manner controlled by the spatial location of the mouse. The sweep gain between frequency and position was randomized from trial to trial so that the same frequency occurred at different spatial locations across trials (see Methods). Mice must attend to the tone and lick at the closest water port whenever the target frequency (22 kHz) is reached. Return runs without a tone served as the control. Incorrect licks led to cessation of the tone and required the mouse to return to the home port to initiate a new trial. Thus, during tone trials, spatial (room) coordinates were uninformative because tones were the only predictor of reward location. Mice reached approximately 70% performance within 3 weeks (Fig. 1b–d and Extended Data Fig. 1b,c). Mice performed best at the nearest target port but roughly equally across the other ports (Fig. 1e,f). Most errors involved the mice licking one port sooner than

¹Neuroscience Institute, New York University Grossman School of Medicine, New York, NY, USA. ²Center for Neural Science, New York University, New York, NY, USA. ³Center for Data Science, New York University, New York, NY, USA. ⁴Center for Computational Neuroscience, Flatiron Institute, New York, NY, USA. ✉e-mail: gyorgy.buzsaki@nyumc.org

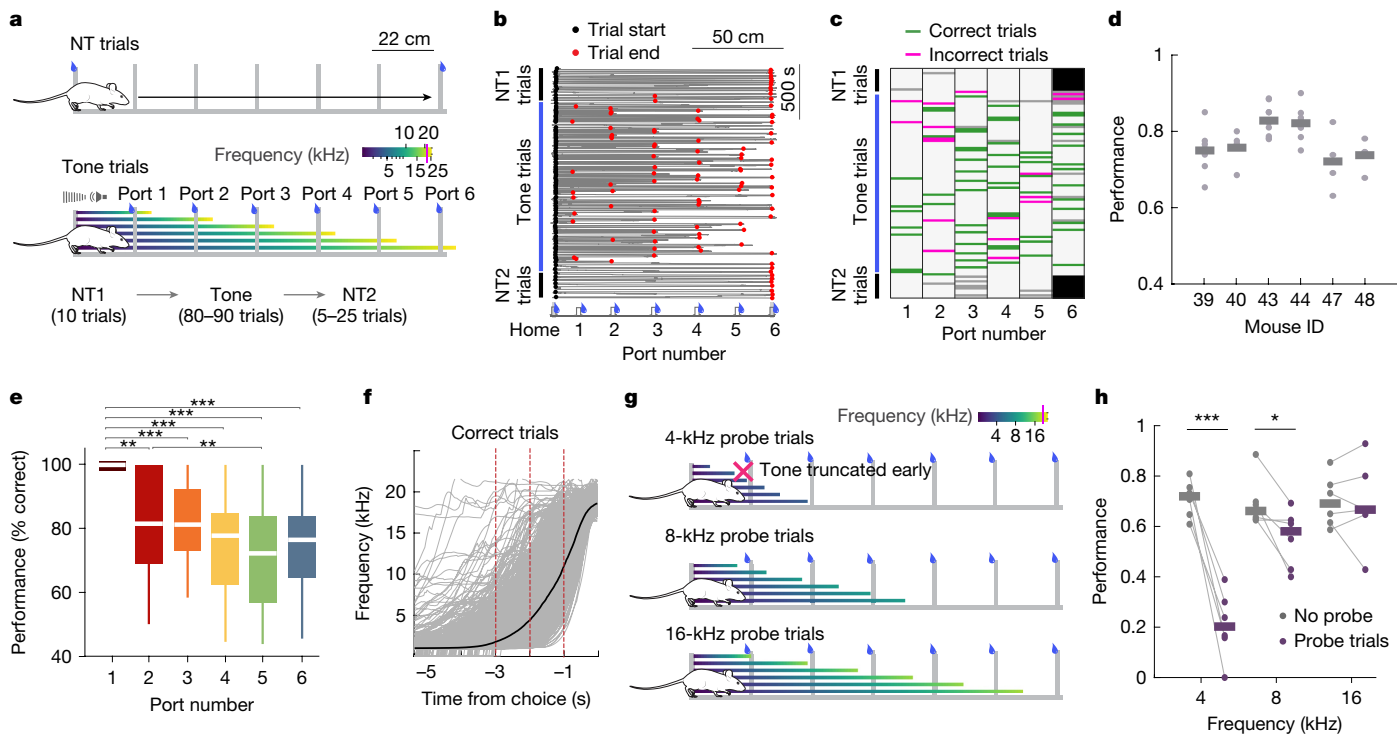


Fig. 1 | Agency-controlled auditory navigation task. **a**, Tone trials were preceded and followed by blocks of no-tone (NT) trials. During tone trials, the tone frequency was controlled by the spatial location of the mouse in a closed-loop manner. Gradient lines (blue to yellow; frequency sweep; 0–25 kHz) correspond to changing frequency (target of 22 kHz, the pink line in the colour map). **b**, Trajectory of a mouse from an example session. During tone trials, mice would either run back to the home port or sample successive ports before returning. The black circles denote the trial start; the red circles indicate the trial end (see Supplementary Videos 1 and 2). **c**, Licks at various ports (black denotes no-tone licks; green indicates tone-correct licks; magenta refers to tone-incorrect licks; and grey denotes other licks). **d**, Fraction of correct trials (median is denoted by the line, and individual sessions are indicated by dots) from six mice. **e**, Percentage of correct trials related to specific ports ($n = 37$ sessions from 6 mice; Friedman test followed by Tukey–Kramer two-sided

post-hoc tests, Chi-squared ($5, 175$) = $64.31, P = 1.55 \times 10^{-12}$). **f**, Mouse-controlled tone frequency progression of each trial (grey lines) in time. The average is denoted in black. The red dashed lines mark -3 s, -2 s and -1 s before the first lick. **g**, Random probe trials were interspersed with tone trials. Frequencies were cut-off at 4, 8 or 16 kHz. Within a session, only one frequency cut-off was used. The mouse schematics in panels **a,g** were created using SciDraw (<https://scidraw.io>) under a Creative Commons licence CC BY 4.0 (credit E. Tyler and L. Kravitz)⁵¹. **h**, Performance during 4-kHz, 8-kHz and 16-kHz probe trials (two-sided paired *t*-test, $n = 6$ sessions from 2 mice, 4 kHz: $t(5) = 8.3014, P = 4.14 \times 10^{-4}$; 8 kHz: $t(5) = 3.0758, P = 0.0276$; 16 kHz: $t(5) = 0.2694, P = 0.7984$). * $P < 0.05$, ** $P < 0.01$ and *** $P < 0.001$. All boxplots show median \pm interquartile; the whiskers show the range excluding outliers in all figures unless otherwise mentioned.

the target, and very few overshoots occurred beyond the target port (Extended Data Fig. 1d,e).

To confirm that mice attended to the auditory tones throughout the run, we implemented probe trials in two mice. Here the tones would abruptly truncate at either 4, 8 or 16 kHz, allowing us to estimate when the mice could successfully extrapolate the slope of the frequency change and predict the target port (Fig. 1g). Probe trials were randomly interspersed with tone trials at a likelihood of approximately 27%. Although performance deteriorated at 4 kHz and 8 kHz, the 16-kHz probe trials were similar to controls, but there was variation in this performance across different ports (Fig. 1h and Extended Data Fig. 1f–h). Thus, on average, mice could estimate and plan their approach to the target port between 8-kHz and 16-kHz tones.

Non-spatial and spatial cell assemblies

Mice were implanted with 128-site double-sided silicon probes in the CA1 pyramidal cell layer²¹. We recorded a median of 235 neurons per session (83–372 cells; 8,113 cells total with $n = 6$, 2,220 pyramidal cells and $n = 1,893$ putative interneurons out of 37 sessions in 6 mice). We first examined the activity dynamics of individual neurons as mice were solving the task. There were clear examples of cells whose discharge ramped up (Fig. 2a, cell 1) or down (Fig. 2a, cell 2) before the approach to any water port during tone trials. For descriptive purposes only,

these neurons are referred to as tone cells based on a detected field in frequency space³ (see Methods). In addition to this non-spatial frequency field, several cells displayed combinations of tone responses and a separate spatial place field (Extended Data Fig. 2a). Although tone cell fields tiled the entire frequency landscape, there was a general overrepresentation of frequencies near the 22-kHz target (Fig. 2b). Tone cells constituted a significant fraction of all recorded CA1 cells (approximately 24% of a median of 132 active pyramidal neurons per session; a total of 1,129 cells; Extended Data Fig. 2b,c). Although many tone cells (such as cell 1) tended to have low-firing rates during no-tone trials, approximately 50% of these cells also had stable place fields during no-tone trials (Extended Data Fig. 2d,e). During error trials, we observed that the firing of tone cells was driven by the approach of the mouse to its chosen port rather than the assigned target for the trial (Extended Data Fig. 2f–h), suggesting that such firing might reflect activity ramping up to the mouse-selected port (that is, the progression to the chosen port of the mouse) rather than auditory frequencies.

In addition to tone cells, there were clear examples of cells firing in fixed spatial coordinates regardless of the choice of the mouse and auditory tones (Fig. 2a, cell 3, and Extended Data Fig. 2a,i). Upon closer inspection, these place cells were also modulated by the approach of the mouse to different ports during tone trials. During tone trials, several cells shifted or expanded their place fields with varying run lengths (Extended Data Fig. 2j,k). These results suggest that rather

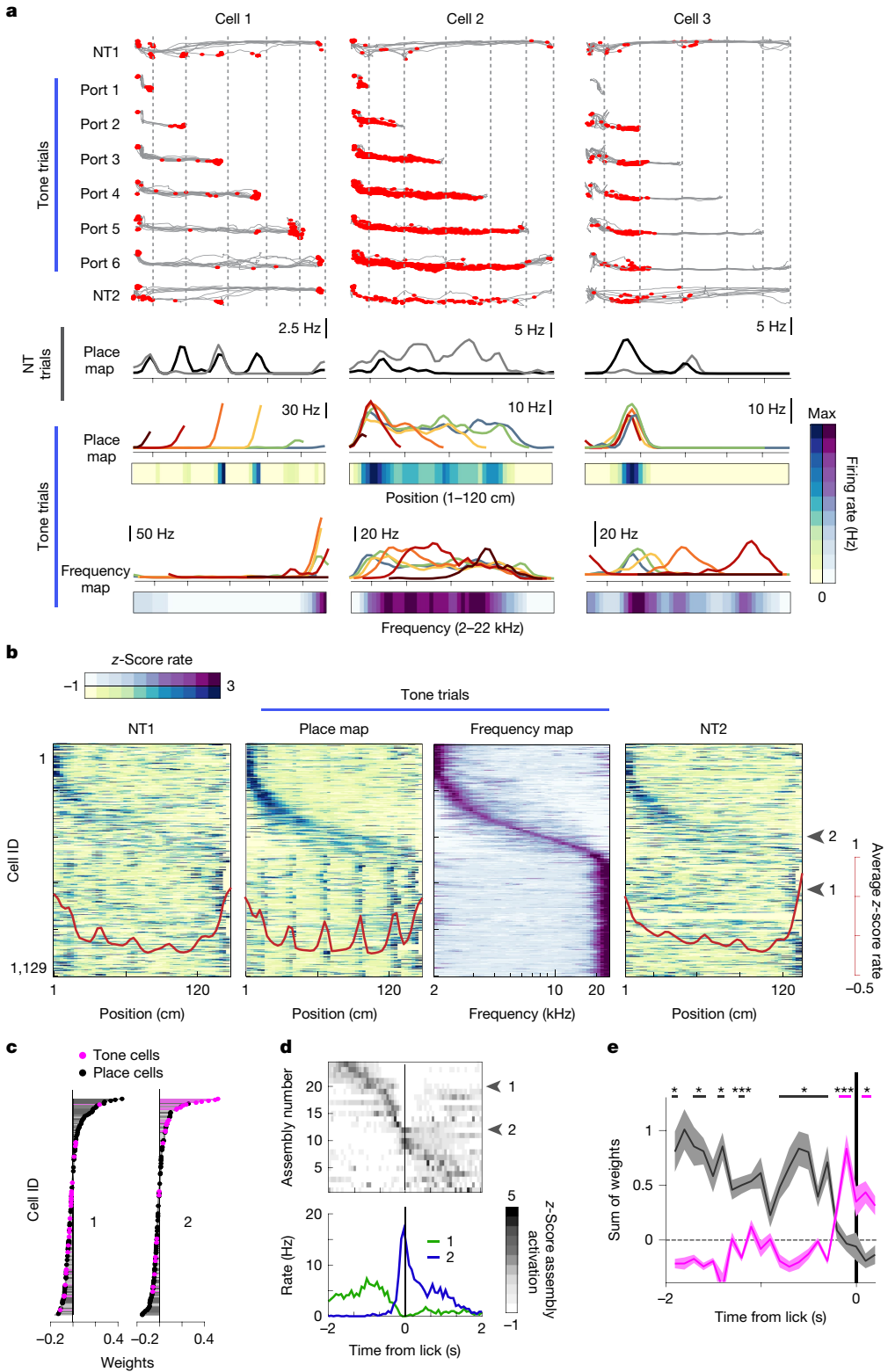


Fig. 2 | Conjunctive non-spatial and spatial neuronal responses. **a**, Three example CA1 pyramidal cells displaying tone (left), mixed (middle) and place (right) tuning. Trajectories (grey lines) by trial type (top; correct trials only are shown, and spikes are overlaid in red), and the average firing rates as heatmaps with respect to position (place map) and frequency (frequency map) for no-tone and tone trials (bottom) are shown. The rainbow spectrum refers to trial types for ports 1–6. **b**, Tone cells, ordered by frequency preference. Tone cells also showed faint port modulation during no-tone trials. Cells 1 and 2 from panel **a** are highlighted (arrowheads). **c**, The relative weights of neurons for two example assemblies, detected using ICA. Grey refers to other cells. Assemblies 1 and 2 are dominated by place and tone cells, respectively. **d**, Activation profile

of all assemblies from an example session against the first detected lick during tone trials (top). Peri-stimulus time histogram (PSTH) of activation around the lick time specifically for assembly 1 (green) and assembly 2 (blue) is also shown (bottom). **e**, Sum of weights of place cells (black) and tone cells (pink) averaged by the time bin of peak activation of each assembly against the first lick. Assemblies active early in a trial were place cell dominated (black line). Assemblies preceding the lick (vertical black line) were tone cell dominated (pink line; $n = 33$ sessions from 6 mice; Wilcoxon two-sided signed-rank test, maximum P value in each block = $0.0273, 0.0332, 0.0234, 2.4 \times 10^{-4}, 0.0371, 4.185 \times 10^{-4}$ and 0.0269). Grey dashed horizontal line, equal contribution of place and tone cells. * $P < 0.05$ and *** $P < 0.001$. Data are shown as mean \pm s.e.m.

Article

than belonging to unique functional cell classes, both tone cell and place cell neurons can have mixed spatial and non-spatial properties.

To quantify to what extent cells were co-modulated by space and progression to the chosen port, we used a Poisson generalized additive model (P-GAM; see Methods), which modelled the average response of a neuron as a function of continuous behaviour variables such as spatial position during no-tone and tone trials and the progression to the choice port (or tone frequency; Extended Data Fig. 3). Almost 60% of the cells were co-tuned to both position and tone frequency (Extended Data Fig. 3f). The ratio of the mutual information for position versus frequency revealed a continuous distribution (Extended Data Fig. 3h,i), establishing that rather than existing as discrete functional classes, most cells exhibited tuning preferences lying along a continuum. Consistent with this idea, place cells and tone cells displayed prototypical properties of hippocampal cells, such as theta-phase precession (Extended Data Fig. 4) and theta compression, with place and tone cells co-firing within the same theta cycle (Extended Data Fig. 5).

Given the mixed nature of neuronal responses, we identified assemblies of co-firing neurons using independent component analysis that were not limited to functionally defined classes (see Methods). Approaches to distinct ports were associated with similar assembly sequences, but the target warped their temporal dynamics (Extended Data Fig. 6a,b). Linking these assemblies back to functional types, we observed that assemblies active early in a trial contained mostly place cells, whereas those at the end mainly contained tone cells (Fig. 2c–e).

In addition to modulation of hippocampal firing between different tone trials, we also observed significant remapping from no-tone 1 (NT1) to tone trials, but not during return runs (Extended Data Fig. 6c–f), indicating context-dependent hippocampal patterns. To address the source of remapping, we trained a separate cohort of mice (range of neurons 59–194 cells; 2,049 cells total with $n = 1,718$ pyramidal cells and $n = 331$ putative interneurons out of 16 sessions in 3 mice) on a control task in which the reward was kept fixed to the end port even during tone trials (Extended Data Fig. 6g–i). Therefore, auditory sweeps were identical but had no task-related significance. As expected, there was a time-proportional drift in neuronal firing throughout the session, yet no remapping was observed between NT1 and tone trials (Extended Data Fig. 6j–l). Thus, sound alone could not explain the remapping.

Mice ran stereotyped trajectories during no-tone trials, mainly along the wall of the track without water ports. By contrast, during tone trials and the second block of no-tone trials, the running trajectories were consistently closer to the wall with middle ports, reflective of the search by the mouse for the correct ports (Extended Data Fig. 7a,b). We regarded the linear track as two-dimensional space and examined the impact of minor deviations. A similar decorrelation was observed between NT1 and tone trials in the two-dimensional maps (Extended Data Fig. 7c–e). We hypothesized that the sequence of positions (where the mice are coming from or are planning to go) was responsible for the decorrelation. We used hierarchical clustering (see Methods) to classify the movement trajectories in the forward running direction into two groups: away from the middle water ports (ports 2–5; Extended Data Fig. 7f, grey lines) or closer to the middle water ports (Extended Data Fig. 7f, black lines). Rate maps, averaging trials for each movement trajectory group and condition (tone versus no tone), were separately generated and correlated. Different movement trajectories yielded significantly different firing patterns within the same task conditions (Extended Data Fig. 7g,h). However, even the same trajectories but in different conditions led to remapping (Extended Data Fig. 7g,h), pointing to the impact of task engagement to remapping.

Effect of external variables on firing

Examination of error trials revealed that firing was not driven by auditory tones but rather by the choice of the mouse. Nonetheless, it is

possible that tone cell firing reflected the ‘belief’ of the mouse or falsely perceived tones. We thus examined the activity of tone cells during probe trials, in which the tone ramp was terminated at 4 kHz. Despite the truncated auditory cue, tone cells continued to ramp after the termination of the tone while the mouse approached the port (Fig. 3a–c). The spatial map, cell assemblies and neural sequences also remained stable despite the truncation of auditory cues (Extended Data Fig. 8). Thus, neuronal firing was not induced and sustained by sound per se. Instead, the findings can be more parsimoniously explained by an internally generated sequence towards an upcoming choice.

We observed no reliable relationship between firing rates and speed (Extended Data Fig. 9j–l), suggesting that tone cells were not modulated by speed. Because most tone cells fired immediately before approaching a water port, we next considered whether they were directly responding to the presence of the reward^{2,22}. However, we found no difference between correct (water reward delivered) and incorrect (no water reward delivered) trials up to the first detected lick (Extended Data Fig. 9a). To further explore the extent to which rewards, or their expectation, might affect firing, we compared firing patterns on return runs. Throughout training, mice were rewarded at the home port only if the trial was correct and unrewarded after incorrect choices. Despite the expectation of the reward presumably being different between correct and incorrect trials, we observed no differences in cell firing on the return runs (Extended Data Fig. 9h,i). To follow up on these results, we designed a new task. Mice were trained to run back and forth on a linear track with a reward port only at one end (666 cells total with $n = 527$ pyramidal cells and $n = 139$ putative interneurons in 2 sessions of 2 mice), therefore never having received a reward at the other end. Midway through the session, rewards were provided at both ends of the track (Fig. 3d). No changes in hippocampal firing were observed upon the introduction of the reward (Fig. 3e–g and Extended Data Fig. 10), suggesting a limited direct influence of rewards on hippocampal firing.

Finally, we asked whether the expectation of reward altered firing patterns by separating the type of licks the mouse performed. We grouped licks into five classes (Fig. 3h–m): (1) ‘choice licks’, the first detected lick on a tone trial, which included both error and correct licks; (2) ‘no-tone licks’, the licks at port 6 during no-tone trials; (3) ‘spontaneous forward licks’, mice sometimes sampled other ports during the no-tone trials or after choosing in tone trials; these spontaneous licks had no associated tasks, tones or rewards and may have reflected exploration or validation; (4) ‘spontaneous reverse licks’, same as type (3) but occurred as the mouse returned to the home port, meant to control for running direction and stereotyped motor movements; and (5) ‘home port licks’, the first lick detected at the home port that initiated the subsequent trial. Spontaneous (exploration) licks were preceded by ramp firing similar to choice licks (Fig. 3k and Extended Data Fig. 9d,e). Only weak responses were observed for no-tone licks, and the smallest response was for homeport licks, suggesting that firing was not a uniform reward-expectation signal but distinct between habitual and task-modulated licks. During tone trials, neuronal responses were not uniformly distributed across the approaches to all ports. Because the number of possible options sequentially decreased with every port crossed, the probability of a correct choice increased for later ports. Spiking preceding licking at earlier (low-probability) ports was stronger, and progressively diminished for later (high-probability) ports (Fig. 3m and Extended Data Fig. 9f,g). Neuronal firing, therefore, reflected a prediction signal for evolving action outcomes, modulated by expectation, similar to the postulated role of dopamine^{23,24}.

Population activity and behavioural goals

To understand how the combined firing of neurons could be related to behavioural decisions, we examined hippocampal firing across the population. The activity of all recorded cells was binned into 100-ms

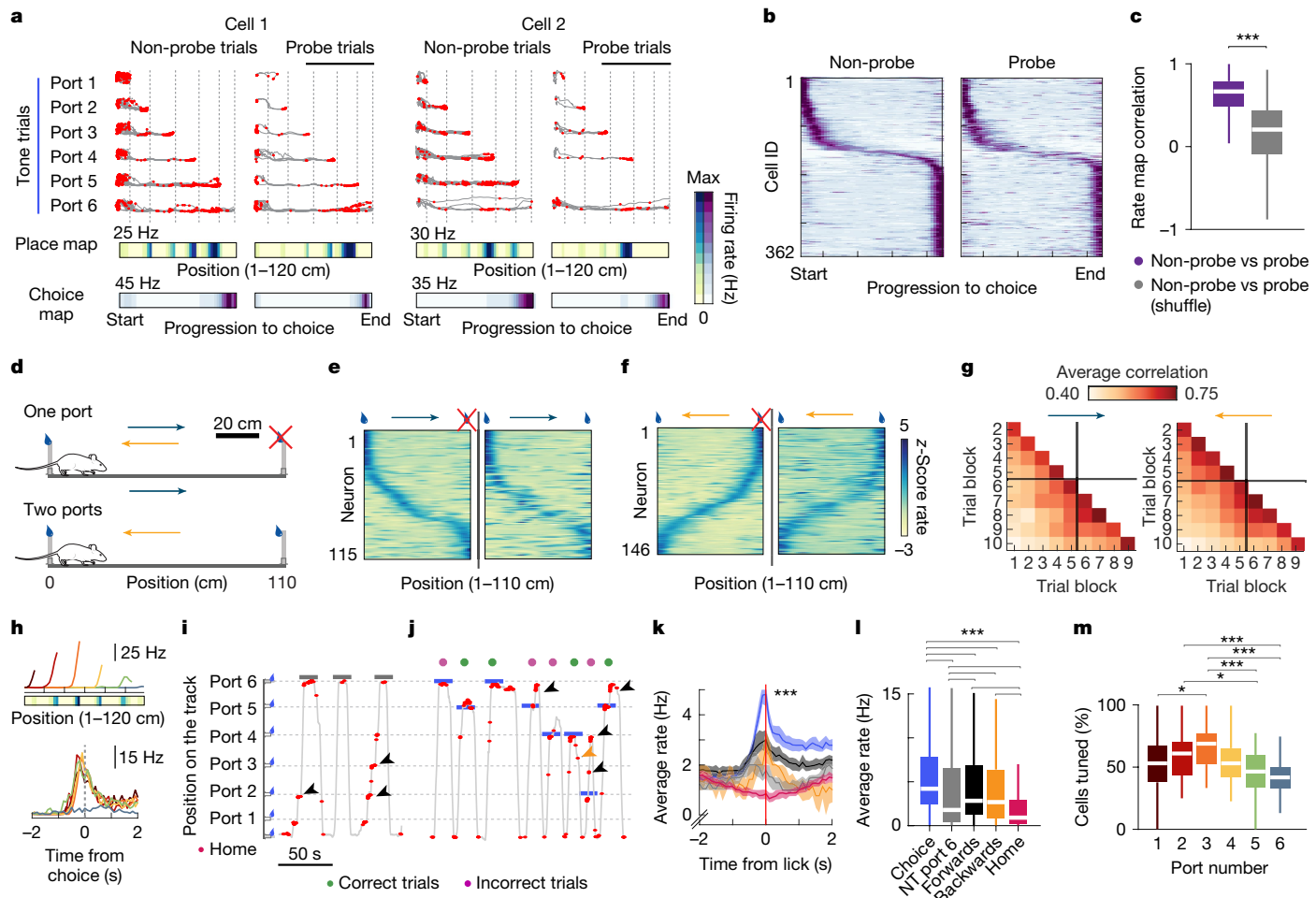


Fig. 3 | Non-spatial firing is not driven by tones or rewards. **a**, Example CA1 pyramidal tone cells during non-probe and probe trials (truncated at 4 kHz). Probe trials were restricted to target ports 3–6 (top black line). Progression to choice refers to the normalized distance to the choice port. **b**, Tone cells sorted by tuning location during non-probe trials (also see Extended Data Fig. 8). **c**, Cell-by-cell correlations for the cells in panel **b** compared with the shuffled data (grey). Activity remained stable despite the termination of the auditory tone ($n = 362$ cells, 8 sessions in 2 mice; Wilcoxon two-sided rank sum test, $z = 23.23, P = 2.09 \times 10^{-19}$). **d**, Lack of reward effect on hippocampal firing. For 40–60 trials, only one end was rewarded, with a second reward introduced for another 40–60 trials. The mouse schematics in panel **d** were created using SciDraw (<https://scidraw.io>) under a Creative Commons licence CC BY 4.0 (credit E. Tyler and L. Kravitz)⁵¹. **e**, Place cells sorted on the one-port condition (left) and maintained between conditions (right). **f**, Same as panel **e** but for return runs. **g**, Cell-by-cell correlation of rate maps for cells in panels **e,f** for 10-trial blocks. The reward was introduced after block 5. **h**, PSTH of a tone cell with respect to the time from the lick from ports 1 to 6. **i**, Spiking activity

of the cell in panel **h** during no-tone trials. The black arrowheads denote spontaneous licks at the middle ports (forward run). **j**, Same as panel **i** during correct (green) and incorrect (pink) tone trials. The blue lines indicate the port the mouse licked. The black arrowheads denote spontaneous licks (that is, sampling other ports after the mouse has already chosen for that trial, ‘fowards’). The yellow arrowhead refers to spontaneous licks in return runs (‘backwards’). **k**, Average PSTH of reward-related tone cells, separated by lick types in panels **i,j**. Statistical comparison as in panel **l**. Colours are as in panel **l**. The lines show median \pm bootstrapped confidence intervals. **l**, Average rate of the cells in panel **k** within ± 0.3 s around the first lick ($n = 565$ –633 cells from 6 mice; Kruskal–Wallis test followed by Tukey–Kramer two-sided post-hoc tests, Chi-squared (4, 3,079) = 330.897, $P = 2.33 \times 10^{-70}$). **m**, Fraction of cells per session firing significantly before the approach to ports 1–6 (rainbow shades) during tone choice licks ($n = 37$ sessions from 6 mice; Friedman test followed by Tukey–Kramer two-sided post-hoc tests, Chi-squared (5, 180) = 35.44, $P = 1.23 \times 10^{-6}$). * $P < 0.05$, ** $P < 0.01$ and *** $P < 0.001$. Boxplots show median \pm interquartile; the whiskers show the ranges excluding outliers.

time bins and visualized by the dimensionality reduction technique uniform manifold approximation and projection (UMAP). Each population vector time bin on this lower-dimension manifold was colour-coded according to behavioural variables, such as the spatial position or the direction of running (Fig. 4a). The manifold mirrored the geometry of the spatial environment, with unique segregations between forward and reverse runs. By selecting the correct forward runs during tone trials and colouring by spatial position, auditory tones or target ports, we observed that the neural trajectories diverged from the main branch before the mice approached the target port (Fig. 4b and Extended Data Fig. 11). We observed similar results across mice and sessions with varying numbers of simultaneously recorded neurons (Extended Data Figs. 12–14).

To examine how neural firing relates to the branches on the neural manifold, we sorted neurons using an unsupervised clustering analysis (see Methods, ‘Cell sequence visualization using rastermap’; Fig. 4c) and found reliable cell assembly sequences across trial types. To quantify how these assemblies related to the manifold shape, we implemented a two-dimensional Bayesian decoder (see Methods) to simultaneously predict the position of the mouse and the chosen port (‘goal’) in 10-ms time bins. Each analysis method, including the UMAP display, cell sequences and Bayesian decoding, showed a similar evolution of neural activity for port-specific runs, including error probe trials (Fig. 4d,e and Extended Data Fig. 15). Specifically, the chosen port by the mouse could be predicted for 85% of trials, approximately 1.1 s before the lick (Extended Data Fig. 16a–d). To relate this decoding

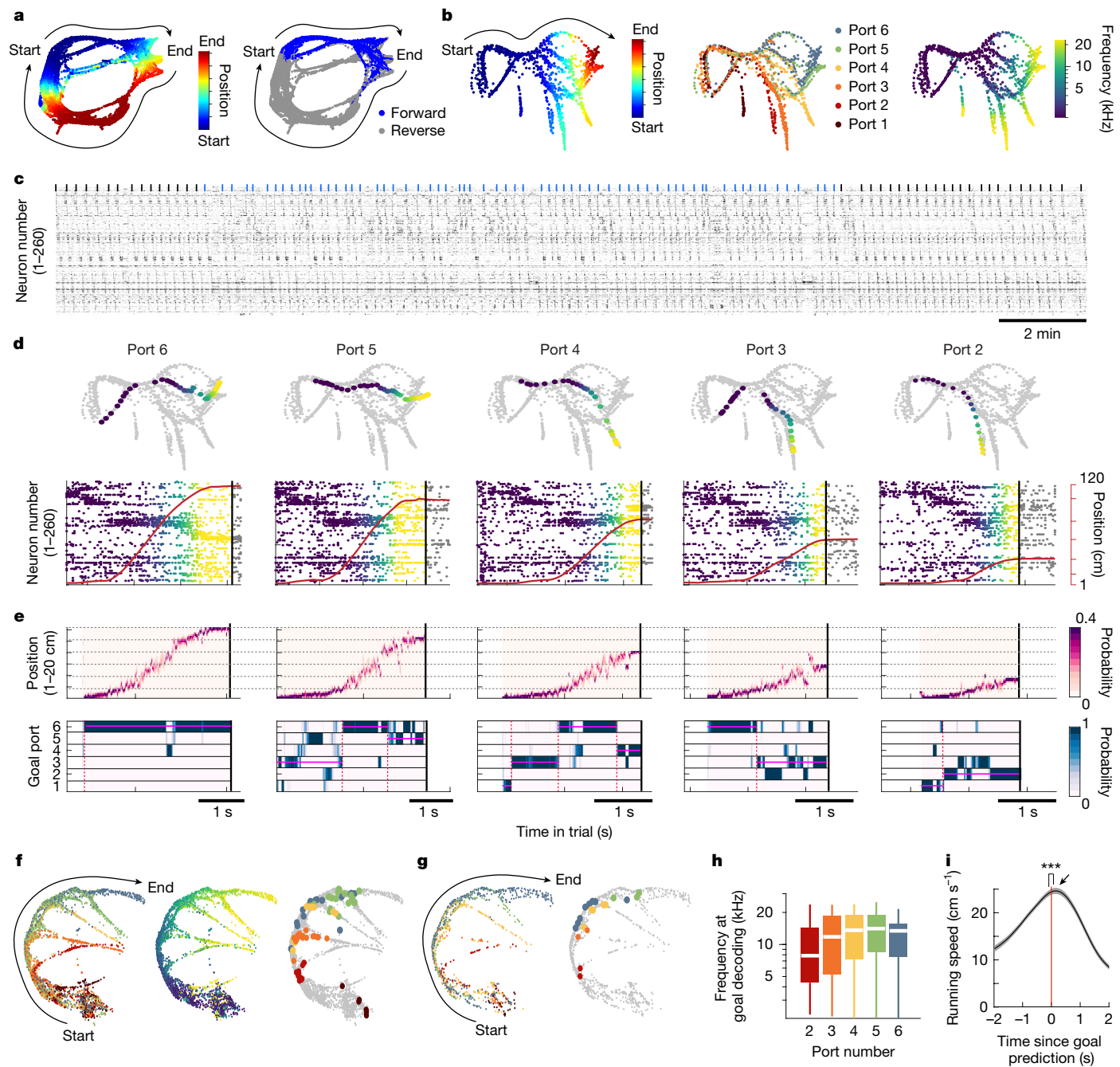


Fig. 4 | Hippocampal CA1 activity predicts upcoming choices. **a**, Neuronal activity in a session ($n = 372$ cells) binned into 100-ms time bins and visualized on a neural manifold (UMAP). The dots denote bins coloured by the position (left) or running direction (right). In panels **a**–**e**, the same session was used. **b**, Manifold constructed from forward runs of correct tone trials, coloured by position (left), target port (middle) and auditory frequency (right). **c**, Spike raster of pyramidal cells, sorted by raster map (see Methods). The ticks denote the start of no-tone (black) and tone (blue) trials. **d**, UMAP (grey dots) overlaid with single trials (top). The colours denote the auditory frequency (the colour map is the same as in panel **b**). Spike rasters, sorted as in panel **c** and coloured by tone frequency, are also shown (bottom). The black vertical line denotes the first lick, and the red line indicates the position of the mouse. **e**, Position decoding (top). The horizontal dashed lines denote port locations 1–6. Goal decoding is also shown (bottom). The black vertical line indicates the first lick;

the red vertical dashed lines refer to significant change points (see Methods); and the pink horizontal line denotes the mode goal decoded between two change points. **f**, UMAP for a different mouse, coloured by the target port (left), tone frequency (middle) and timestamp of the final change point during correct trials (right). The colours denote trial ports 1–6. Decoding fell on the branch points for each target on the manifold. **g**, Same as panel **f**, but for 4-kHz probe trials. **h**, Average tone frequency at which the decoder settled onto its final change point to correctly predict the target, separated by port ($n = 158$ –346 decoded trials; compare with Fig. 1h and Extended Data Fig. 1). Boxplot shows median \pm interquartile; the whiskers show the range excluding outliers. **i**, Goal decoding ($t = 0$, vertical red line) preceded the running speed peak (arrow; $n = 37$ sessions from 6 mice). Data are shown as mean \pm s.e.m. (comparison between 66 ms before and after $t = 0$, Wilcoxon two-sided signed-rank test, $P = 2.69 \times 10^{-4}$).

time point to branches on the neural manifold, we used a change-point detection algorithm (see Methods) to identify consistent epochs of decoding prediction. The time point of the last-detected epoch

generally occupied the branch points of the manifold for each port (Fig. 4f,g and Extended Data Fig. 1e). The average tone frequency at this time point was between 8 kHz and 12 kHz (Fig. 4h), corresponding

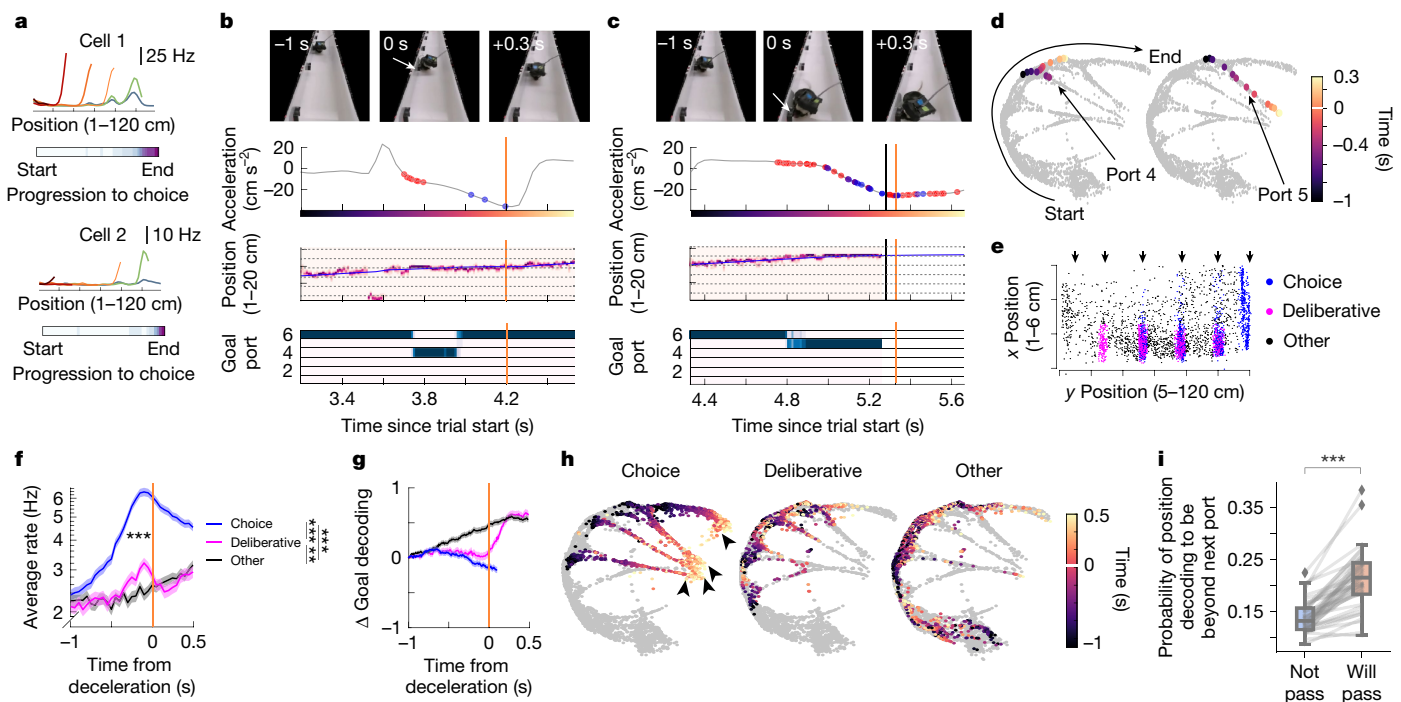


Fig. 5 | Action plan decoding in single trials. **a**, Two example tone cells. Spatial firing (top) and average progression-to-choice map (bottom) are shown. **b,c**, Example events from a single trial, showing behavioural ‘checking’ of port 4 (**b**; white arrow; no lick at the port) and licking at correct port 5 (**c**). Row 1 shows frames from a front camera. Row 2 displays the acceleration profile (the yellow line indicates the acceleration minimum). The red and blue dots are spikes from cells 1 and 2 in panel **a**. Row 3 shows the position decoding. The blue line denotes the position of the mouse. Row 4 shows goal decoding. The black vertical line in panel **c** shows the time of choice lick (see also Supplementary Video 3). **d**, UMAP display (as in Fig. 4f) for the single trial shown in panels **b,c**. The coloured dots denote the time windows shown in panels **b,c**. **e**, Significant decelerations during the forward runs (all mice), clustered into three categories: choice decelerations (blue), deliberative decelerations (pink) and all other decelerations (‘Other’, black). Only ports 3–6 were considered to allow for deliberation at previous ports. Arrows, port locations. **f**, Average tone cell

firing around each of the detected deceleration moments ($n = 633$ cells), comparing firing rates between -100 ms and 0 ms; Friedman test followed by Tukey–Kramer two-sided post-hoc tests, Chi-squared ($2, 1,264$) = 399.23 , $P = 2.04 \times 10^{-87}$). **g**, Change in goal decoding compared with the predicted goal at -1 s. Note the sudden shift in goal prediction for deliberative decelerations. Vertical line, time of deceleration peak. **h**, Significant decelerations, separated by category on the UMAP. Arrowheads, chosen ports 3–6. **i**, The probability of the position decoder predicting a location beyond the upcoming port was significantly higher if the mouse eventually crossed the port (will pass) versus if it licked at the port (not pass). This reflects a ‘lookahead’ beyond the current location, based on the target port of the mouse (Wilcoxon two-sided signed-rank test $P = 2.91 \times 10^{-11}$). The lines denote individual sessions (37 sessions, 6 mice). Boxplot shows median \pm interquartile; the whiskers show the range excluding outliers. *** $P < 0.001$.

to the frequencies when the mice predicted the target port on probe trials (Fig. 1h). Decoding preceded changes in running speed (Fig. 4i). Thus, the goal-specific modulation of place and tone cells led to a population-level code that corresponded to the upcoming actions of the mouse.

Within-trial evolution of action plan

We reasoned that if hippocampal activity reflected action plans, we could trace how such action plans are shaped within a trial (Fig. 5a–d and Supplementary Video 3). We identified moments of peak deceleration in the speed profile of the mouse when it approached the chosen port or crossed previous ports (Fig. 5e and Extended Data Fig. 17a,b). These transient deceleration events were often accompanied by brief head turns towards the port under consideration (termed ‘deliberation’; Fig. 5b and Supplementary Video 3). During deliberative but not during other decelerations on the track, tone cells briefly ramped their activity but quickly stopped spiking, corresponding to the mouse passing the port (Fig. 5b,c,f), which was also accompanied by a sudden jump in goal decoding and flickering of tone cell assemblies (Fig. 5b,c,g and Extended Data Fig. 17c,d). Although choice decelerations deeply extended into the manifold branches, deliberation neural trajectories only briefly entered the relevant manifold branch and exited back out (Fig. 5d,h). In addition, the likelihood of the position of the mouse

being decoded beyond the next port was significantly higher if the mouse was going to pass an upcoming port – an effect that was not dependent on the speed of the mouse but on its position ‘lookahead’^{25,26} during the ascending phase of the theta cycle (Fig. 5i and Extended Data Fig. 17e–i). Thus, goal-specific signals were modified dynamically with ongoing action plans.

Discussion

We studied how hippocampal neurons vary their apparent tuning to various modalities in a paradigm where space, auditory tones, rewards and contexts were juxtaposed. We observed correlations between firing patterns versus spatial position, time, auditory modalities, reward and context. Yet, in agreement with experiments that attempted to identify modality-specific or abstract space responses^{1–8,27,28}, we found that the dominance of particular correlations depends on task demands and, therefore, varies across experiments. Analysis of the movement paths of the mice uncovered that hippocampal firing was linked to prospective action patterns and modulated by goal expectation rather than tuning to the relevant sensory modalities. We hypothesize that the previously reported apparent hippocampal tuning to abstract cognitive variables^{1–8,27,28} can be grounded in a framework in which neuronal firing reflects an internally generated action plan afforded by the environmental conditions of the mouse.

Article

Although adjusting the target frequency of the discriminative sound by the mouse was a critical task variable, our analysis revealed that it was not the ‘sound landscape’³ that brought about the firing changes of hippocampal neurons but, instead, the specific actions taken by the mouse. First, tone-responding neurons increased their discharge at sampled water-port locations during no-tone trials. Second, during error trials, the firing pattern of the neurons reflected the progression of the mouse towards the erroneously chosen port rather than the auditory frequencies. Third, when the tone ramp was terminated at 4–16 kHz on probe trials, neuronal firing continued to ramp similarly as the mouse approached the port. Finally, the firing patterns of hippocampal neurons ‘remapped’²⁹ across tone and no-tone trials of the main task. Yet, the presence of the same auditory sweep with no consequence on securing the reward had no effect on neuronal firing in control experiments³. We hypothesize that the role of the discriminative ‘go’ signal is to select an action sequence with an associated neuronal trajectory, which proceeds according to internally organized motives, possibly modified during learning, rather than continuously controlled by sensory cues. How learning shapes such internal dynamics remains an interesting question for future studies.

An alternative explanation of our findings is that neuronal trajectories were influenced and scaled by the presence of the reward and its expectation^{2,22}. Consistent with this idea, hippocampal neurons started to ramp up their firing rates before licks, independent of the location of the mouse on the track or the presence of a tone. Yet, control experiments distinguished firing pattern correlates of reward and sensory cues from motor responses at both the single-neuron and the population levels. First, the ramping of lick-responding neurons was identical during rewarded and either erroneous or learned non-rewarded trials, demonstrating that reward expectation and consumption were not critical. Second, in the tone task, neurons that robustly responded before licking also responded before exploratory licks but only weakly in the no-tone task despite involving the same motor patterns. Conversely, very few tone cells responded before home port licks, even though they resulted in the same volume of water as rewarded tone or no-tone trials. In addition, the fraction of responding neurons and the magnitude of the responses were different between ports. Finally, tone cells fired even during hesitation or deliberation without licks. Thus, neither the reward per se nor the simple motor information could explain hippocampal neuronal firing patterns, which are better explained by deliberative and intentional actions towards goals.

Several observations support the action plan hypothesis. Sequences of cell assemblies consistently evolved approximately 1 s before the choice, including probe trials. Early in the trial, assemblies were dominated by place cells and gradually replaced by tone cells. Although these labels approximate the experimenter-established relationships, they do not imply distinct mechanisms. We observed reliable goal decoding and branches on the manifold emerging at a similar timescale, coinciding with the approximate frequency at which mice made decisions. Together, our findings align better with an interpretation that the discriminative signal selected a neuronal sequence (or trajectory), which proceeded according to internally organized motives that guided the current action plan of the mouse. This view is supported by the observation that the hippocampus continues to generate the same fractions of place cell sequences even in the absence of the grid cell-supporting medial entorhinal input^{30–33}. Building on previous research³⁸, we hypothesize that external cues do not continuously drive neuronal spikes in the hippocampus³³ but rather serve to select and update pre-existing (or attractor) trajectories appropriate to a given task phase.

The hypothesis of neuronal sequence-sustained internal goals is supported by previous observations demonstrating that the extent and forms of neuronal sequences in the hippocampus correlate with the direction and distances of the animal-set goals^{8,25,28,34,35}. Our findings are also relevant to rescaling place cells with changes in the size of

the environment³⁶ and the intrinsic switching of their fields between reference frames^{37–40}, as well as to goal-predicting ‘splitter’ cells and prediction in general^{25,41,42}. Each of these independently studied features may reflect the same underlying physiological mechanism if hippocampal firing is viewed from the lens of a dynamical sequence generator that progresses towards a task-related goal^{43–46}. Although our results primarily pertain to non-spatial aspects of firing, we hypothesize that similar action sequences may also underlie spatial firing that is sensitive to precise trajectories and the goals of the animal^{38,47}. In our experiments, the evolving internal goals were reflected by the quantal jumps of the population activity from port to port and associated behavioural deliberations (brief head movements) of the mouse (Supplementary Video 3).

The concept of a goal expands beyond a mere physical location and encompasses any inherent end point that leads to a desired outcome, as implied by experiments in humans^{48,49}. Despite the vagueness of these terms, the distinction between reward and goal is subtle yet crucial, shifting the focus from an external stimulus or location to an internally driven, intentional and deliberative target^{8,50}. Departing from the notion of ‘representation’ of external stimuli or ‘mapping’ the environment onto the hippocampus, we hypothesize that its internally generated dynamics are projected onto the niche of the animal to make sense of the world through its prospective actions.

Online content

Any methods, additional references, Nature Portfolio reporting summaries, source data, extended data, supplementary information, acknowledgements, peer review information; details of author contributions and competing interests; and statements of data and code availability are available at <https://doi.org/10.1038/s41586-024-08397-7>.

1. MacDonald, C. J., Lepage, K. Q., Eden, U. T. & Eichenbaum, H. Hippocampal ‘time cells’ bridge the gap in memory for discontiguous events. *Neuron* **71**, 737–749 (2011).
2. Gauthier, J. L. & Tank, D. W. A dedicated population for reward coding in the hippocampus. *Neuron* **99**, 179–193.e7 (2018).
3. Aronov, D., Nevers, R. & Tank, D. W. Mapping of a non-spatial dimension by the hippocampal–entorhinal circuit. *Nature* **543**, 719–722 (2017).
4. Manns, J. R., Howard, M. W. & Eichenbaum, H. Gradual changes in hippocampal activity support remembering the order of events. *Neuron* **56**, 530–540 (2007).
5. Josselyn, S. A. & Tonegawa, S. Memory engrams: recalling the past and imagining the future. *Science* **367**, eaaw4325 (2020).
6. Tuncdemir, S. N. et al. Parallel processing of sensory cue and spatial information in the dentate gyrus. *Cell Rep.* **38**, 110257 (2022).
7. Purandare, C. & Mehta, M. Mega-scale movie-fields in the mouse visuo-hippocampal network. *eLife* **12**, RP85069 (2023).
8. Radvansky, B. A., Oh, J. Y., Climer, J. R. & Dombeck, D. A. Behavior determines the hippocampal spatial mapping of a multisensory environment. *Cell Rep.* **36**, 109444 (2021).
9. O’Keefe, J. & Krupic, J. Do hippocampal pyramidal cells respond to nonspatial stimuli? *Physiol. Rev.* **101**, 1427–1456 (2021).
10. Eichenbaum, H. A cortical–hippocampal system for declarative memory. *Nat. Rev. Neurosci.* **1**, 41–50 (2000).
11. Vanderwolf, C. H. Hippocampal electrical activity and voluntary movement in the rat. *Electroencephalogr. Clin. Neurophysiol.* **26**, 407–418 (1969).
12. Arezzo, J. & Vaughan, H. G. Cortical potentials associated with voluntary movements in the monkey. *Brain Res.* **88**, 99–104 (1975).
13. Numan, R. A prefrontal–hippocampal comparator for goal-directed behavior: the intentional self and episodic memory. *Front. Behav. Neurosci.* **9**, 323 (2015).
14. Miller, E. K. & Cohen, J. D. An integrative theory of prefrontal cortex function. *Annu. Rev. Neurosci.* **24**, 167–202 (2001).
15. Olton, D. S., Becker, J. T. & Handelmann, G. E. Hippocampal function: working memory or cognitive mapping? *Physiol. Psychol.* **8**, 239–246 (1980).
16. McNaughton, B. L. et al. Deciphering the hippocampal polyglot: the hippocampus as a path integration system. *J. Exp. Biol.* **199**, 173–185 (1996).
17. Stachenfeld, K. L., Botvinick, M. M. & Gershman, S. J. The hippocampus as a predictive map. *Nat. Neurosci.* **20**, 1643–1653 (2017).
18. Buzsáki, G. & Moser, E. I. Memory, navigation and theta rhythm in the hippocampal–entorhinal system. *Nat. Neurosci.* **16**, 130–138 (2013).
19. Schiller, D. et al. Memory and space: towards an understanding of the cognitive map. *J. Neurosci.* **35**, 13904–13911 (2015).
20. Lisman, J. et al. Viewpoints: how the hippocampus contributes to memory, navigation and cognition. *Nat. Neurosci.* **20**, 1434–1447 (2017).
21. Huszár, R., Zhang, Y., Blockus, H. & Buzsáki, G. Preconfigured dynamics in the hippocampus are guided by embryonic birthdate and rate of neurogenesis. *Nat. Neurosci.* **25**, 1201–1212 (2022).

22. Sosa, M., Plitt, M. H. & Giocomo, L. M. Hippocampal sequences span experience relative to rewards. Preprint at *bioRxiv* <https://doi.org/10.1101/2023.12.27.573490> (2023).
23. Syed, E. C. J. et al. Action initiation shapes mesolimbic dopamine encoding of future rewards. *Nat. Neurosci.* **19**, 34–36 (2015).
24. Bogacz, R. Dopamine role in learning and action inference. *eLife* **9**, e53262 (2020).
25. Wikenheiser, A. M. & Redish, A. D. Hippocampal theta sequences reflect current goals. *Nat. Neurosci.* **18**, 289–294 (2015).
26. Kay, K. et al. Constant sub-second cycling between representations of possible futures in the hippocampus. *Cell* **180**, 552–567.e25 (2020).
27. Sun, C., Yang, W., Martin, J. & Tonegawa, S. Hippocampal neurons represent events as transferable units of experience. *Nat. Neurosci.* **23**, 651–663 (2020).
28. Nieh, E. H. et al. Geometry of abstract learned knowledge in the hippocampus. *Nature* **595**, 80–84 (2021).
29. Muller, R. U. & Kubie, J. L. The effects of changes in the environment on the spatial firing of hippocampal complex-spike cells. *J. Neurosci.* **7**, 1951–1968 (1987).
30. Hales, J. B. et al. Medial entorhinal cortex lesions only partially disrupt hippocampal place cells and hippocampus-dependent place memory. *Cell Rep.* **9**, 893–901 (2014).
31. Ormond, J., McNaughton, B. L. & Moser, E. I. Place field expansion after focal MEC inactivations is consistent with loss of Fourier components and path integrator gain reduction. *Proc. Natl Acad. Sci. USA* **112**, 4116–4121 (2015).
32. Robinson, N. T. M. et al. Medial entorhinal cortex selectively supports temporal coding by hippocampal neurons. *Neuron* **94**, 677–688.e6 (2017).
33. Zutshi, I., Valero, M., Fernández-Ruiz, A. & Buzsáki, G. Extrinsic control and intrinsic computation in the hippocampal CA1 circuit. *Neuron* **110**, 658–673.e5 (2022).
34. Pastalkova, E., Itskov, V., Amarasingham, A. & Buzsáki, G. Internally generated cell assembly sequences in the rat hippocampus. *Science* **321**, 1322–1327 (2008).
35. Green, L., Tingley, D., Rinzel, J. & Buzsáki, G. Action-driven remapping of hippocampal neuronal populations in jumping rats. *Proc. Natl Acad. Sci. USA* **119**, e2122141119 (2022).
36. Diba, K. & Buzsáki, G. Hippocampal network dynamics constrain the time lag between pyramidal cells across modified environments. *J. Neurosci.* **28**, 13448–13456 (2008).
37. Muzzio, I. A. et al. Attention enhances the retrieval and stability of visuospatial and olfactory representations in the dorsal hippocampus. *PLoS Biol.* **7**, e1000140 (2009).
38. Jackson, J. & Redish, A. D. Network dynamics of hippocampal cell-assemblies resemble multiple spatial maps within single tasks. *Hippocampus* **17**, 1209–1229 (2007).
39. Fenton, A. A. & Muller, R. U. Place cell discharge is extremely variable during individual passes of the rat through the firing field. *Proc. Natl Acad. Sci. USA* **95**, 3182–3187 (1998).
40. Kentros, C. G., Agnihotri, N. T., Streater, S., Hawkins, R. D. & Kandel, E. R. Increased attention to spatial context increases both place field stability and spatial memory. *Neuron* **42**, 283–295 (2004).
41. Frank, L. M., Brown, E. N. & Wilson, M. Trajectory encoding in the hippocampus and entorhinal cortex. *Neuron* **27**, 169–178 (2000).
42. Wood, E. R., Dudchenko, P. A., Robitschek, R. J. & Eichenbaum, H. Hippocampal neurons encode information about different types of memory episodes occurring in the same location. *Neuron* **27**, 623–633 (2000).
43. Whittington, J. C. R. et al. The Tolman–Eichenbaum machine: unifying space and relational memory through generalization in the hippocampal formation. *Cell* **183**, 1249–1263.e23 (2020).
44. El-Gaby, M. et al. A cellular basis for mapping behavioural structure. *Nature* <https://doi.org/10.1038/s41586-024-08145-x> (2024).
45. Villette, V., Malvache, A., Tressard, T., Dupuy, N. & Cossart, R. Internally recurring hippocampal sequences as a population template of spatiotemporal information. *Neuron* **88**, 357–366 (2015).
46. Buzsáki, G. & Tingley, D. Space and time: the hippocampus as a sequence generator. *Trends Cogn. Sci.* **22**, 853–869 (2018).
47. Liberti, W. A., Schmid, T. A., Forli, A., Snyder, M. & Yartsev, M. M. A stable hippocampal code in freely flying bats. *Nature* **604**, 98–103 (2022).
48. Schacter, D. L. & Addis, D. R. On the nature of medial temporal lobe contributions to the constructive simulation of future events. *Phil. Trans. R. Soc. B* **364**, 1245–1253 (2009).
49. Wikenheiser, A. M. & Redish, A. D. Decoding the cognitive map: ensemble hippocampal sequences and decision making. *Curr. Opin. Neurobiol.* <https://doi.org/10.1016/j.conb.2014.10.002> (2014).
50. Hok, V. et al. Goal-related activity in hippocampal place cells. *J. Neurosci.* **27**, 472–482 (2007).
51. Tyler, E. & Kravitz, L. Walking mouse. *Zenodo* <https://doi.org/10.5281/zenodo.3925915> (2020).

Publisher's note Springer Nature remains neutral with regard to jurisdictional claims in published maps and institutional affiliations.

Springer Nature or its licensor (e.g. a society or other partner) holds exclusive rights to this article under a publishing agreement with the author(s) or other rightsholder(s); author self-archiving of the accepted manuscript version of this article is solely governed by the terms of such publishing agreement and applicable law.

© The Author(s), under exclusive licence to Springer Nature Limited 2025

Article

Methods

Experimental animals

The Institutional Animal Care and Use Committee at New York University Langone Medical Center approved all experiments. Mice were housed in fully equipped facilities in the New York University School of Medicine Science Building. Mice were housed at around 22 °C, with a relative humidity of approximately 45%. The mice were on a 12-h light-dark cycle and were housed 4–5 per cage before implantation. Upon the onset of behavioural training and subsequent surgery, the mice were moved to a 12-h reverse light cycle (lights on or off at 19:00 or 07:00, respectively) and housed individually. Mice were provided food and water ad libitum but were water restricted to maintain 80% of their weight during and after behavioural training. We used a combination of transgenic and wild-type male mice (auditory task; $n = 6$ male mice, of which 4 were double transgenic mice crossed between *Pvalb*-IRES-Cre females (Jax Stock no. 017320) and Ai32 males (Jax Stock no. 024109); the other two mice were C57BL/6J wild types (Jax Stock no. 000664); and for the control task, $n = 3$ male mice of which 1 was double transgenic as described above, and 2 were wild type). No obvious differences in behaviour or neural firing emerged between the two types of mice. At the time of implantation, mice ranged from 3 to 6 months of age and 22–31 g in weight. For the variable reward task, $n = 2$ male mice of which both were double transgenic as described above.

Surgical procedures

Mice were implanted with 128-channel silicon probes (ASSY-INT128, Diagnostic Biochips) into CA1 (for task mice, one mouse was implanted with a P128-6 probe, whereas five mice were implanted with P64-1-D Janus double-sided probes; for control mice, one mouse was implanted with a P128-6 probe, whereas two mice were implanted with P64-1-D Janus double-sided probes). For all surgical procedures, mice were induced with 2.5–3% isoflurane in oxygen anaesthesia (SomnoSuite Low-Flow Anesthesia System) and placed in a stereotaxic apparatus (Kopf Instruments). The level of isoflurane was then decreased to 1.3–1.5% for the remaining surgical procedures. During the surgery, body temperature was maintained at 37 °C using a heating pad (Physitemp, TCAT-2LV Animal temperature controller). Vaseline was applied as eye lubricant. Following no reaction to toe pinch, a small incision was made in the scalp, the scalp was cleaned with iodine (Dynarex Povidine Iodine solution) and lidocaine cream (Ferndale LMX4) was locally applied. The skull was then scored using a scalpel to ensure adhesion to the headcap. The coordinates used for CA1 were –1.9 mm anteroposterior and +1.6 mm mediolateral from bregma. A ground screw coupled with a 0.005" stainless steel wire (792800, A-M Systems) was implanted in the skull above the cerebellum. Next, a base plate was cemented to the scored skull surface using Metabond (S380, Parkell C&B). The probes were mounted on custom-made metal microdrives to allow precise adjustment of vertical position of sites after implantation⁵². During surgery, probes were implanted at the level of the cortex (0.4 mm dorsoventral). A combination of mineral oil (O121-1, Fisher Chemical) and paraffin wax (18634, Sigma-Aldrich; melted in a 1:1 ratio) was used to seal the craniotomy and cover the probe shanks. In the transgenic mice, four 200-μm optic fibres were also implanted in the brain, but sessions when those stimulations were performed were not included in this paper. The microdrive was cemented on the metabond skull surface using a combination of light-cured and regular dental cement (Unifast LC, Unifast Trad). Finally, a custom 3D-printed grounded copper mesh hat was constructed⁵², shielding the probes. Following surgery, an NSAID analgesic was injected (Ketoprofen at 5 mg kg^{−1}, approximately 0.13 ml for a 25 g mouse, stock solution of 1 mg ml^{−1}, subcutaneous). Mice were allowed to recover and were continuously monitored for at least 1 week before water restriction and behavioural training resumed. Body weight was monitored for all the days following surgery.

The position of the probe was confirmed at the end of each experiment. The mice were perfused with cold saline solution (0.9%) followed by pre-made 4% paraformaldehyde in PBS solution (Affymetrix USB). Brains were post-fixed for 24 h in 4% paraformaldehyde and sectioned coronally to visualize the hippocampus. Sections were obtained with 40–50 μm thickness using a vibrating blade microtome (VT1000S, Leica), mounted on electrostatic slides, coverslipped with DAPI Fluoromount-G (0100-20, Southern Biotech), and imaged using a virtual slide microscope (VS120, Olympus). No additional immunohistochemistry or tissue processing was done to visualize the probe tracks.

Behavioural apparatus and task description

We constructed a linear track using white acrylic (1/8" thick) with dimensions of 120 cm (length) × 7.5 cm (width), with 5-cm high walls. The track contained seven equally spaced (20 cm apart) water ports. The home port and port 6 were located on the short walls of the track, whereas ports 1–5 were located along one of the long walls of the track. Water was delivered through blunt 18-G needles connected (using Tygon E-3603 Tubing; 1/16" ID, 1/8" OD) to solenoid valves (EW-98302-02, Cole-Parmer) that were briefly opened for 30 ms. The needle was positioned precisely within a U-shaped infrared (IR) sensor (HiLetgo LM393 Correlation Photoelectric Sensor), such that any licks on the needle would break the IR beam. Successive breaks at the same port during a visit were disregarded during analysis. A speaker (MakerHawk Mini Speaker, 3 W 8Ω) was positioned above port 6, facing the home port, and was calibrated to ensure that it played frequencies up to 25 kHz (60–80 dB SPL; 20 dB roll-off between 2 kHz and 25 kHz).

Water delivery and the tones were controlled by a combination of Bonsai (<https://bonsai-rx.org/>) and a custom-made Arduino circuit. A Basler overhead camera (acA640-90gc, Graftek Imaging) acquired images with a frame rate of 30 Hz. Bonsai was used to detect the real-time position of the mouse by contrasting the black fur of the mouse against the white maze. This centroid position was sent to Arduino using the serialStringWrite function. The Arduino would randomly assign a target port for a trial and rescale the Bonsai-detected position of the mouse to the distance between the home and the target port. For example, if the target port was 6 (located 120 cm from the start location), and the current position of the mouse was at 60 cm, the instantaneous normalized position was 60/120, that is, 0.5. However, if the target port was 4 (located 80 cm from the start location), the normalized position became 60/80, that is, 0.75. Auditory frequencies were linked to this normalized position according to the following formula:

$$F = f_0 \cdot \left(\frac{f_{\text{target}}}{f_0} \right)^x \quad (1)$$

where, F = current frequency, $f_0 = 2$ kHz, $f_{\text{target}} = 22$ kHz and x is the current normalized position. The frequency sweep was designed to increase logarithmically from 2 kHz (similar to ref. 3), with the target port coinciding with a frequency of 22 kHz. Although tones could continue beyond the target, because of the limitations of the speaker, frequencies beyond 25 kHz were not accurately delivered if the mouse overshot, but these were rare instances. Tones were delivered using the Arduino Tone() function, which generated square pulses modulated at the specified frequency. Microphone (AU-PM422, MAONO; sampling rate up to 192 kHz) recordings ensured that auditory frequencies were playing as designed and the resultant sound spectrogram was inspected using Audacity.

Acoustic cue-guided navigation paradigm. During no-tone trials, mice ran along the linear track, receiving water at the two ends of the track, that is, port 6 and the home port. In the tone trials, licking at the home port initiated a tone of 2 kHz that ascended logarithmically in a closed loop with the position of the mouse. A correct lick response triggered the solenoid, and the tone stopped playing. We ensured

that the delay between the mouse touching the spout and the transistor-transistor logic (TTL) pulse of the lick was not greater than 33 ms (corresponding to 1 frame-rate cycle of the Arduino) and corrected this delay in our analysis. After a choice, mice were free to sample other ports (unrewarded checks) before returning to the home port to lick to initiate the next trial. If the previous trial was correct, mice also received a water reward at the home port. However, if the previous trial was incorrect, both the choice lick and the subsequent home port lick were unrewarded. An incorrect lick response in the tone trials was followed by a 1-s long 3-kHz error tone.

Probe trials. In two mice, probe trials were randomly interspersed with regular (non-probe) trials at approximately 30% probability, but only if the target was port 3, 4, 5 or 6. This criterion was introduced because ports 1 and 2 did not allow enough separation in terms of distance between the truncation of tones and the target port. Within a session, a cut-off frequency was pre-determined as 4 kHz, 8 kHz or 16 kHz, after which tones stopped playing with a trial. A correct probe trial was if the mouse correctly extrapolated the sweep speed and licked at the target based on the short, truncated sweep. Other licks were classified as incorrect. For electrophysiological recordings, only 4-kHz probe trials were used to maximize the duration when sounds were off.

Control task paradigm. To control for auditory cues, three mice were trained to run back and forth on the same track with the same task structure as previously described. However, only the two ports at either end were rewarded. Tones would stop playing after 25 kHz. Return runs did not have any tones associated with them. For comparison with the mice performing the task, recordings were only analysed after mice had been performing the control version of the task for at least 7 days. This ensured that there were no effects due to the novelty of the auditory cue and that mice had learned that the tones were irrelevant.

Variable reward paradigm. Mice had previously been trained to run in the auditory navigation task. After collecting data on that task, mice were kept in their home cage for 3–4 weeks. They were then introduced to a novel linear track of similar dimensions (110 cm long, 6 cm wide). Recordings were analysed on the first day of this task. For the first approximately 60 trials, only one end was rewarded. Midway through the task, and without interruptions, a second reward was introduced at the opposite end of the track.

Behavioural training and analysis

On days when behavioural sessions were performed, the mice were deprived of water and only received water during the sessions. On other days, the mice were provided 2 ml of water. Body weight was monitored on all days, and the water schedule was interrupted if the body weight reached below 80% of the starting weight. Before implantation, mice were pre-trained to perform the task until they reached 65% accuracy. The stages of training included: (1) habituation to the track and water ports, so that mice learned to poke to trigger water rewards (approximately 2 days). (2) Linear track training in which mice received a water reward at either end after poking and reached up to 60–70 trials (approximately 3–4 days). (3) Autoshaping, in which tones would increase in a closed loop to the position of the mouse, but the water reward would automatically be released at the target port without the mice having to nose poke. Incorrect licks were also not penalized (approximately 2 days). (4) Training to abstain from licking at incorrect ports. Only one port was assigned the target in this stage, generally port 3. Mice must poke at the target to receive water rewards, and licks at earlier ports would result in incorrect trials. This would often be the most variable stage between mice. If mice did not adapt their behaviour after 100 trials, the first few ports would be physically blocked to train the mice to abstain from premature licks (approximately 3–4 days). (5) Expanding phase 4 to a few more ports, usually ports 1–3, or ports 3

and 6 (3–4 days). (6) The final version of the task with all ports rewarded (approximately 3–4 days). Mice transitioned between stages 4 and 6 if they reached 65% at each stage. The entire training from start to finish would usually take approximately 3 weeks. Following surgery, mice were retrained starting from stage 4 but would quickly transition to stage 6 within 3–4 days.

To quantify the performance of the mice, the proportion correct and proportion incorrect was calculated for each target port separately. The performance was calculated as the fraction of correct licks at a given port relative to the total number of trials where that was the target port. The proportion of incorrect trials was calculated as the fraction of trials when a given port was incorrectly chosen relative to all trials where that port was not the target.

Electrophysiological recordings, unit clustering and neuron classification

Electrophysiological data were acquired using an Intan RHD2000 system (Intan Technologies) digitized at 30 kHz. The wideband signal was downsampled to 1,250 Hz and used as the local field potential. A pulley system was designed to counteract the weight of the tether and headstage. The position of the mouse was recorded using an overhead Basler camera (acA1300-60 gmNIR, Graftek Imaging) sampling at 30 Hz. A front camera recorded the forward running direction of the mouse for additional behavioural analysis (see Supplementary Videos 1 and 3). Camera videos were synchronized with neural data with TTLs signalling shutter position. Digital inputs to the Intan RHD system provided timestamps for TTLs from lick ports and water delivery from the solenoids.

Spikes were extracted and classified using Kilosort⁵³ using a custom pipeline KilosortWrapper (<https://github.com/brendonw1/KilosortWrapper>). Automated sorting was followed by manual curation of the waveform clusters using Phy (<https://github.com/cortex-lab/phy>) and custom plugins for Phy (<https://github.com/petersenpeter/phy1-plugins>). Kilosort clustering was performed with the following parameters: ops.Nfilt:6*numberChannels, ops.nt0:64; ops.whitening:'full';ops.nSkipCov:1;ops.whiteningRange:64;ops.criterion:NoiseChannels:0.00001; ops.Nrank: 3; ops.nfullpasses: 6; ops.maxFR: 20000; ops.fshigh: 300; ops.ntbuff: 64; ops.scaleproc: 200; ops.Th: [4 10 10]; ops.lam: [5 20 20]; ops.nannealpasses: 4; ops.momentum: 1./[20 800]; ops.shuffle_clusters: 1. Units were separated into putative pyramidal cells and narrow waveform interneurons using their autocorrelograms, waveform characteristics and firing rate. This classification was performed using CellExplorer⁵⁴.

Rate map generation

1D spatial rate maps were generated by binning spiking data into 2.5-cm wide bins, generating maps of spike counts and occupancy for periods when the speed of the mouse was more than 0.1 cm s^{-1} . A rate map was constructed by dividing the spike map by the occupancy map and smoothing it with a 5-bin Gaussian filter [0.02 0.1 0.16 0.1 0.02]. For tone trials, forward direction maps used time windows between the start of the trial (home port lick) and the end of the trial (first detected lick on the trial). Maps for the reverse direction runs included time windows between the end of a trial (first detected lick) and the subsequent home port lick. Because the mouse behaviour was more variable during the return runs, an additional speed criterion was applied (speed $< -2 \text{ cm s}^{-1}$) to ensure movement in the reverse direction.

1D frequency or choice maps were constructed by rescaling the spatial position of the mouse to match the trajectory length within a trial, calculated as: (instantaneous spatial position/distance of the relevant port for that trial from the home port).

The relevant port was generally considered to be the port where the mouse first licked but was the assigned target port for the error trial analysis in Extended Data Fig. 2. For frequency maps, frequency was estimated using equation (1). Rate maps were generated as described above but by binning spikes along the choice variable

Article

(bin size, 2.5% normalized distance to the choice port, also becomes a frequency map in the logarithmic scale). For tone trials, average maps for ports 1–6 were first constructed separately, and then these average maps were averaged further to generate overall tuning across tone trials.

2D spatial maps were generated by making 1-cm wide bins and binning across both the x and the y spatial positions. Smoothing involved a 5×5 bin Gaussian filter [0.0025 0.0125 0.0200 0.0125 0.0025; 0.0125 0.0625 0.1000 0.0625 0.0125; ... 0.0200 0.1000 0.1600 0.1000 0.0200; ... 0.0125 0.0625 0.1000 0.0625 0.0125; ... 0.0025 0.0125 0.0200 0.0125 0.0025].

Field detection

Place cells. Place fields were defined from the above-described rate maps using a combination of peak detection and across-trial correlation methods. Only pyramidal cells were used. The field boundaries were defined for cells with a minimum peak firing rate of 5 Hz, and extended until the rate was above 20% of the peak firing rate. The width of the field was required to be between 8% and 70% of the size of the rate map (between 10 cm and 87.5 cm for place cells, and between 1.6 kHz and 14 kHz for tone cells). All cells that had a detected field using these criteria in spatial rate maps were included as place cells in Extended Data Fig. 2i.

For the place field modulation by run length analysis shown in Extended Data Fig. 2, cells were only included if they had a place field in the rate map generated by averaging across port 2–6 tone trials as well as a field within 30 cm of this averaged field for each individual trial type.

For the correlation metrics across no-tone and port 6 tone conditions, such as Extended Data Fig. 6, as well as the trajectory analysis in Extended Data Fig. 7, cells were included if they had a field in either no-tone or port 6 tone maps. Spatial rate map correlations for individual cells between conditions were calculated as the average pixel-by-pixel Pearson correlation coefficient of the smoothed-averaged firing rate maps. Rate map stability was defined by generating rate maps for the first and second halves of each condition and correlating these half-session rate maps.

The same analysis and field criterion were used for animals trained on the variable reward port task. For the correlation between the one-port and two-port rewarded conditions, cells were included if they had a field in either map.

Tone cells. For tone cells, cells were selected with the same criteria as place cells to have a field in the averaged frequency maps. To ensure that these cells were firing robustly across trials, the frequency maps across ports 1–6 were correlated to each other and additionally required a correlation value > 0.1 . For reward responses, peri-event time histograms around lick events were generated separately for each port for tone cells by binning spike rates in 100-ms bins. To focus on cells firing around the reward location, only cells with a field within the last 10 bins were used for the analysis. Speed analysis was performed by calculating the instantaneous firing rate of tone cells within 100-ms bins and calculating the Pearson's correlation coefficient of the rate with running speed.

Movement trajectory clustering

The movement trajectory of the mice along the width of the track was clustered by using agglomerative hierarchical clustering⁴⁷. The x position along the width of the track within a trial was downsampled to 7 points (each point corresponding to the y position of a water port) for all no-tone and port 6 tone trials (total of n trials). This $n \times 7$ array representing individual x position trajectories was clustered into paths according to their Euclidean distance using the linkage ('complete') and cluster functions in MATLAB. Only a maximum of two clusters was allowed. Two sets of average rate maps were therefore generated for each condition (NT1, port 6 tone and NT2) by combining all trials

classified within each cluster separately. We also generated within cluster, within condition maps by dividing trials by half, thus estimating baseline stability. These sets of rate maps were then correlated within and across conditions.

Poisson generalized additive model

To estimate the tuning of each neuron to each variable, we used a P-GAM^{55,56}. The P-GAM defines a non-linear mapping between spike counts of a unit y_t and a set of continuous variables x_t and discrete events z_t . For our model, we selected continuous and discrete covariates: (1) the spatial position in the forward runs of the no-tone trials, (2) the spatial position in the forward runs of the tone trials, (3) the spatial position in the return runs of all trials, and (4) the progression to the chosen port (progression to choice, or c) during tone trials, calculated as, $p = (\text{instantaneous spatial position}/\text{distance of the chosen port for that trial from the home port})$. To directly compare kernel strengths between (2) and (4), the progression-to-choice variable was rescaled to the range of 0–120 cm (ref. 57). Finally, (5) the discrete covariate included the timestamps for the first lick for every port visit throughout the session.

The spike rates, continuous and discrete covariates were binned at a 33-ms resolution (30-Hz camera frame rate). Next, each tuning function was initialized as a basis set of cubic piecewise polynomials of order 4. The number of piecewise polynomials, or splines, was determined by the number of knots where the polynomials meet. The number of knots was chosen as $k = 5$ by an iterative process to uniformly cover the range of each variable without overfitting. See <https://github.com/BalzaniEdoardo/PGAM> for a tutorial.

The unit log-firing rate of each neuron was estimated as follows:

$$\log(\mu_t) = \sum_{j=1}^{K1} f_j(x_j(t)) + \sum_{i=1}^{K2} f_i * z_i \quad (2)$$

where $f_j(\cdot)$ are non-linear functions of individual continuous input variables $\mathbf{x}(t) \in \mathbb{R}^{K1}$ and discrete input variables $\mathbf{z}(t) \in \mathbb{R}^{K2}$. $*$ is the convolution operator. The spike rate of a neuron was estimated by a Poisson random process.

$$y_t | \mathbf{x}, \mathbf{f} - \text{Poisson}(\mu_t) \quad (3)$$

$f(\cdot)$ was modelled using a penalized spline basis expansion. We used flexible B-splines to define $f(\cdot) = \beta \cdot b(\cdot)$, where b is the basis set as defined by the splines and β is a parameter that defines the weights or kernel strengths for each covariate. To enforce a smooth fit, each spline was associated with a quadratic penalty term $\mathcal{L}(\lambda)$ to control its energy, or 'wigginess'. Both parameters β and the hyperparameters λ are learned from the data by an iterative optimization procedure (see ref. 55). To find the optimal regularization hyperparameter λ , a k-fold cross-validation ($k = 5$) was implemented before fitting the data using the double generalized cross-validation score. For each fold of the fivefold cross-validation, the λ was selected for each neuron from the range of (1.5, 1.75, 2, 2.5, 5). The final value of λ associated with the highest R^2 was chosen to fit the model. The variability of the R^2 values after each fold of the fivefold cross-validation was visually inspected for 40 neurons of one session to ensure that the model fit was not sensitive to the subset of data being fit.

Our model was fit using 90% of the data, whereas neurons with a firing rate below 0.5 Hz were excluded from the fit. After fitting each variable, the model computed the marginal confidence intervals for the contribution of each variable to the neural response. The final values of the kernel strength and the magnitude of the confidence intervals were used to determine whether a variable has a significant contribution to the firing rate of the neuron. This was done using the Farebrothers algorithm, which computes the P values associated with each variable. If the P value was below the threshold of 0.001, then the variable was

considered to contribute to the neural response significantly. After the initial fit of all variables (full model), the non-significant variables were removed from the model and the model was re-fit (reduced model), so that the parameters of only the significant variables were estimated again and more reliably.

In addition to the five variables described above, licks were also separated into five distinct classes as described in the main text (choice, no-tone port 6, spontaneous forward and return, home) and added as variables to the P-GAM fit. The tuning function of each lick class was initialized as a basis set of cubic piecewise polynomials of order 1 and 2 knots that were defined around the lick timestamp. The tuning function of the neuron to each lick class thus resembled a step function with a distinct β , or kernel strength for each type of lick, which allowed us to compare the modulation of the spike rate by lick type (Extended Data Fig. 3j–l).

The mutual information (MI) was computed as the difference between the entropy of unit firing rates $H(y)$ and the entropy of the rate conditioned on a specific variable x , $H(y|x)$, under Poisson noise assumptions. Specifically,

$$I(x_j, y) = H[y] - H[y_t|x_j] = H[y] - \sum_k p_k H[y_t|x_j^k] \quad (4)$$

where $H[y]$ is approximated as the entropy of a Poisson variable with λ equal to the mean firing rate of the unit. For p_k (probability of the stimulus taking value x_j^k), we used the empirical distribution of the discretized stimulus x_j^k . $H[y_t|x_j^k]$ was approximated as the entropy of Poisson random variable with a mean given by the tuning function of the neuron, provided by the P-GAM model.

Theta-phase precession and theta compression

Average rate maps in the place and frequency domain were calculated for all tone trials. Cells with a field in these averaged maps were then independently analysed for fields within 30 cm of the averaged field in trials for ports 2–6 independently. Local field potentials from the stratum oriens was filtered, and the instantaneous phase was determined using a Hilbert transform. Fields were normalized between 0 and 1 to the beginning to the end of each field in either the space or tone domain. A circular-linear regression was generated for spikes occurring within the bounds of the fields, and the slope and significance of the regression line are reported. Significance was achieved by a $P < 0.05$. Boundaries of ± 2 cycles were used to constrain the circular-linear regression.

For theta compression, only averaged rate maps were used. The distance between the field peaks was estimated in either the space or tone domain for cells with overlapping fields. Spike times from pairs of neurons from within the field were cross-correlated with 5-ms bin size, and the peak lag between ± 100 ms was estimated as the temporal lag between the cells.

Assembly analysis

Cell assemblies were defined using an unsupervised statistical framework based on a hybrid principal component analysis followed by ICA^{58,59}. Spike trains of pyramidal neurons were binned in 33-ms intervals, and the matrix of firing correlation coefficients for all pairs of neurons was constructed. Principal components with eigenvalues that exceeded the threshold for random firing correlations (using the Marčenko–Pastur law) were used to determine the number of assemblies. Next, using the fast-ICA algorithm⁶⁰, we determined the vector of weights (contribution of each neuron) for each assembly (component). Place cell and tone cell contributions for each assembly were estimated by averaging the weights of all place and tone cells for each assembly. The strength of activation for each assembly as a function of time was determined by multiplying the convolved z-scored firing rate of a given neuron at a given time by the weight of contribution of that neuron to the assembly. The product of these weighted spike counts was then summed for all non-identical pairs of neurons to generate

the instantaneous activation strength. Activations greater than 1.5 times the standard deviation were used as timestamps of activation of each assembly.

Low-dimensional manifold visualization with UMAP (unsupervised)

The procedure was implemented as previously described⁶¹. In brief, neural spiking data (spike count) during maze running (speed $> 1 \text{ cm s}^{-1}$) were binned into 100-ms bins. The data were then smoothed using a 5-bin (500 ms) wide Gaussian kernel and z-scored. To examine the effect of binning and smoothing, we also performed finer binning (20 ms) and no smoothing (Extended Data Fig. 11). The UMAP dimensionality reduction algorithm⁶² was then applied to the preprocessed data matrix. Each point in the low-dimensional manifold corresponds to the population activity at a single time bin. The UMAP code is available (https://github.com/lmcinnes/umap/blob/master/doc/how_umap_works.rst). The UMAP hyperparameters used were: $n_{\text{neighbors}} = 20$, $\text{metric} = \text{'cosine'}$, $\text{output_metric} = \text{'euclidean'}$, $\text{learning_rate} = 1.0$, $\text{init} = \text{'spectral'}$, $\text{min_dist} = 0.1$, $\text{spread} = 1.0$, $\text{repulsion_strength} = 1.0$, $\text{negative_sample_rate} = 5$, $\text{target_metric} = \text{'categorical'}$, $\text{dens_lambda} = 2.0$, $\text{dens_frac} = 0.3$, $\text{dens_var_shift} = 0.1$.

Cell sequence visualization using rastermap

Neurons were sorted in Fig. 4, Extended Data Figs. 5 and 8 using rastermap⁶³. Only pyramidal cells with an average firing rate of more than 0.1 Hz were included. The same sorting was maintained for all figures. The specific parameters used were, $n_{\text{clusters}} = 50$, $n_{\text{PCs}} = 200$, $\text{locality} = 0$, $\text{time_lag_window} = 3$.

Bayesian decoding

To decode the discretized position and chosen port of the animal at each 10-ms time bin, we used a state-space decoder that is the Bayesian decoder equipped with a causal filter on the posterior^{64,65}, based on specified transition probability on the position and goal⁶⁶. In the encoding stage, the spiking activity of the population was modelled as independent inhomogeneous Poisson processes whose instantaneous rates were functions (tuning curves) of the position of the mouse and the chosen port for the trial. The tuning curves (x) were constructed using a kernel density estimator with a Gaussian kernel of 3 cm for the position dimension and virtually no smoothing for the goal dimension. The state-transition probability $p(x_{t+1}|x_t)$ is the product of the transition probability for each dimension, where the transition in the position follows a Gaussian random walk with a variance of 25 cm^2 per time bin, and the transition in goal follows a sticky uniform prior, where the probability of staying in the current goal is 0.9 per second ($0.9^{\circ}0.01$ per bin), and equal probability for the rest of the available goals (available meaning the goals that are ahead of the current position). The posterior of the state given the history of observations, follows this recursive relationship:

$$p(x_t|s_{1:t}^n) \sim \prod_n p(s_t^n|x_t) \int p(x_t|x_{t-1})p(x_{t-1}|s_{1:t-1}^n)dx_{t-1}$$

where the $p(s_t^n|x_t)$ is the Poisson likelihood function of observing a spike count of s_t^n from neuron n at time t if the state variable is x_t . The normalizer is the integral of the right-hand side with respect to x_t , which is tractable because the state variables are discrete. Once we obtained the joint posterior of position and goal, we marginalized over one variable and analysed the marginal posterior of the other. We adapted the code from the ‘replay_trajectory_classification’ Python library⁶⁷.

Change point detection for goal decoding

To identify consistent epochs of goal decoding while ignoring minor fluctuations, we used the change point detection approach previously developed⁶⁸ called the pruned exact linear time method (a modified version was previously used⁶⁹). In brief, the posterior for goal (marginalized

Article

over position) within a trial was partitioned into segments to minimize the sum of the within-segment variances plus a regularization term.

$$\sum_{i=1}^{m+1} \sum_k \text{Var}(p_{\tau_{i-1+1}: \tau_i}(\text{goal} = k)) + \beta m$$

The regularization term is a penalty coefficient $\beta \times$ the number of change points m . The penalty coefficient was selected heuristically to produce large segments where the goal decoding was mostly stable ($\beta = 20$). Varying the coefficients tended not to change the starting time of the last segment, which was used to project onto the UMAP manifold. The change points $\tau_{1:m}$ (τ_{m+1} defined to be the last time bin) that segment the posterior were found by dynamic programming with pruning⁶⁸. The number of change points was automatically selected by the trade-off between the sum of variances and the regularization. The implementation used the Python library ‘ruptures’.

Deceleration minima

During tone trial forward runs, the acceleration of the mouse was convolved with a 200-ms Gaussian kernel. Using the MATLAB ‘findpeaks’ function, we identified troughs in the acceleration profile (‘MinPeakProminence’, 10). Each deceleration was then labelled as either the final ‘choice’, deceleration close to a port before the final choice (‘deliberation’), or ‘other’ decelerations.

Generalized additive model for theta lookahead

We used a GAM⁷⁰ to predict the sum of the posterior beyond the upcoming port using linear covariates speed and will_pass (whether the animal will pass the upcoming port) and smooth terms position and theta phase.

```
posterior_beyond_upcoming_port  
= speed + will_pass + f(position) + g(theta phase),
```

where, $g(x), f(x) = \sum_{j=1}^m b_j(x)\beta_j$, where $\{b_j(x)\}_j$ is a set of B-spline basis functions, and $\{\beta_j\}_j$ are the coefficients. We used 30 basis functions for the position and five basis functions for the theta phase, both with degree 3. The number of basis functions was heuristically chosen such that the fitted smooth functions were interpretable. Varying the numbers did not change the results regarding the significance of the will_pass term. We used an identity link function and Gaussian noise model. The model is implemented using the Python library statsmodels.

Statistical analysis

Mice from the control paradigm and auditory task paradigm were run in four parallel cohorts. No specific analysis was used to estimate a minimal population sample, but the number of mice, trials and recorded cells were larger than or similar to those used in previous studies^{71–74}. All statistical tests were conducted using MATLAB R2023b, and the details of the tests used are described with the results. Unless otherwise noted, all tests used non-parametric comparisons of means and variance (Wilcoxon paired signed-rank tests, Wilcoxon rank-sum test, Kruskal–Wallis one-way analysis of variance and Friedman tests). When parametric tests were used, the data satisfied the criteria for normality (Kolmogorov–Smirnov test) and equality of variance (Bartlett test for equal variance). All post-hoc tests were performed using Tukey honest significant differences and correcting for multiple comparisons. The boxplots represent the median and 25th and 75th percentiles, and the whiskers represent the data range. In the boxplots without data points, outliers were excluded from the plots but always included in the statistical analysis.

Reporting summary

Further information on research design is available in the Nature Portfolio Reporting Summary linked to this article.

Data availability

The dataset generated for this study has been made publicly available in the Buzsáki laboratory repository (<https://buzsakilab.nyumc.org/datasets/Zutshil/Nature2024/>).

Code availability

All custom data preprocessing code is freely available on the Buzsáki laboratory repository (<https://github.com/buzsakilab/buzcode>). The code for the P-GAM implantation is freely available on GitHub (<https://github.com/BalzaniEdoardo/PGAM>). The scripts specific to analysing this dataset are available on I.Z.’s GitHub (<https://github.com/Ipsita-Zutshi/JungleBook/tree/main/ToneTask>).

52. Vöröslakos, M., Petersen, P. C., Vöröslakos, B. & Buzsáki, G. Metal microdrive and head cap system for silicon probe recovery in freely moving rodent. *eLife* **10**, e65859 (2021).
53. Pachitariu, M., Steinmetz, N., Kadir, S., Carandini, M. & Harris, K. Fast and accurate spike sorting of high-channel count probes with KiloSort. In *Proc. 30th International Conference on Neural Information Processing Systems* Vol. 29 (eds Lee, D. D. et al.) 4455–4463 (Curran Associates, 2016).
54. Petersen, P. C., Siegle, J. H., Steinmetz, N. A., Mahallati, S. & Buzsáki, G. CellExplorer: a framework for visualizing and characterizing single neurons. *Neuron* **109**, 3594–3608.e2 (2021).
55. Balzani, E., Lakshminarasimhan, K., Angelaki, D. E. & Savin, C. Efficient estimation of neural tuning during naturalistic behavior. In *Proc. 34th International Conference on Neural Information Processing Systems* (eds Larochelle, H. et al.) 1057 (Curran Associates, 2020).
56. Noel, J. P. et al. Coding of latent variables in sensory, parietal, and frontal cortices during closed-loop virtual navigation. *eLife* **11**, e80280 (2022).
57. Singh, D. & Singh, B. Investigating the impact of data normalization on classification performance. *Appl. Soft Comput.* **97**, 105524 (2020).
58. Lopes-dos-Santos, V., Ribeiro, S. & Tort, A. B. L. Detecting cell assemblies in large neuronal populations. *J. Neurosci. Methods* **220**, 149–166 (2013).
59. van de Ven, G. M., Trouche, S., McNamara, C. G., Allen, K. & Dupret, D. Hippocampal offline reactivation consolidates recently formed cell assembly patterns during sharp wave-ripples. *Neuron* **92**, 968–974 (2016).
60. Ritchey, M., Libby, L. A. & Ranganath, C. Cortico-hippocampal systems involved in memory and cognition: the PMAT framework. *Prog. Brain Res.* **219**, 45–64 (2015).
61. Yang, W. et al. Selection of experience for memory by hippocampal sharp wave ripples. *Science* **383**, 1478–1483 (2024).
62. McInnes, L., Healy, J., Saul, N. & Großberger, L. UMAP: uniform manifold approximation and projection. *J. Open Source Softw.* **3**, 861 (2018).
63. Stringer, C. et al. Rastermap: a discovery method for neural population recordings. *Nat. Neurosci.* <https://doi.org/10.1038/s41593-024-01783-4> (2024).
64. Johnson, A. & Redish, A. D. Neural ensembles in CA3 transiently encode paths forward of the animal at a decision point. *J. Neurosci.* **27**, 12176–12189 (2007).
65. Johnson, A., Jackson, J. C. & Redish, A. D. in *Information Processing by Neuronal Populations* (eds Holscher, C. & Munk, M.) 95–119 (Cambridge Univ. Press, 2008).
66. Brown, E. N., Frank, L. M., Tang, D., Quirk, M. C. & Wilson, M. A. A statistical paradigm for neural spike train decoding applied to position prediction from ensemble firing patterns of rat hippocampal place cells. *J. Neurosci.* **18**, 7411–7425 (1998).
67. Denovellis, E. L. et al. Hippocampal replay of experience at real-world speeds. *eLife* **10**, e64505 (2021).
68. Killick, R., Fearnhead, P. & Eckley, I. A. Optimal detection of changepoints with a linear computational cost. *J. Am. Stat. Assoc.* **107**, 1590–1598 (2012).
69. Zheng, Z. et al. Perpetual step-like restructuring of hippocampal circuit dynamics. *Cell Rep.* **43**, 114702 (2024).
70. Hastie, T. & Tibshirani, R. Generalized additive models: some applications. *J. Am. Stat. Assoc.* **82**, 371–386 (1987).
71. McKenzie, S. et al. Preexisting hippocampal network dynamics constrain optogenetically induced place fields. *Neuron* **109**, 1040–1054.e7 (2021).
72. Senzai, Y., Fernandez-Ruiz, A. & Buzsáki, G. Layer-specific physiological features and interlaminar interactions in the primary visual cortex of the mouse. *Neuron* **101**, 500–513.e5 (2019).
73. Valero, M. et al. Sleep down state-active ID2/Nkx2.1 interneurons in the neocortex. *Nat. Neurosci.* **24**, 401–411 (2021).
74. Zhang, Y. et al. Cholinergic suppression of hippocampal sharp-wave ripples impairs working memory. *Proc. Natl. Acad. Sci. USA* **118**, e2016432118 (2021).

Acknowledgements We thank R. Kasa and L. Anderson for help with behavioural training; A. Mar for help with the behavioural paradigm design; and S. Sethi and the Buzsáki laboratory for insightful comments throughout the project and suggestions for the manuscript. The mouse schematics in this paper were created using SciDraw (<https://scidraw.io>) under a Creative Commons licence CC BY 4.0 (credit E. Tyler and L. Kravitz)⁵¹. This work has been supported by a Simons Collaboration on the Global Brain Transition to Independence Fellowship to I.Z., the Bodossaki Foundation Scholarship for Postgraduate Studies and the Swiss-European Mobility Program for Worldwide Projects and Traineeships to A.A., a US NIH NINDS grant 1RF1NS12712201 to E.B. and C.S., and NIH grants (R01MH122391 and U19NS107616) and an NSF grant 1707316 (NeuroNex MINT) to E. Yoon and G.B.

Author contributions I.Z. and G.B. planned and designed the experiments. Experiments were performed by I.Z., A.A. and T.D. Data analysis for single cells was performed by I.Z. and A.A. W.Y. performed the UMAP analysis. Z.(S.)Z. performed the position and goal-decoding analysis with support from A.H.W. E.B. and C.S. provided support for the P-GAM implementation. I.Z. and G.B. wrote the paper with input from all authors.

Competing interests The authors declare no competing interests.

Additional information

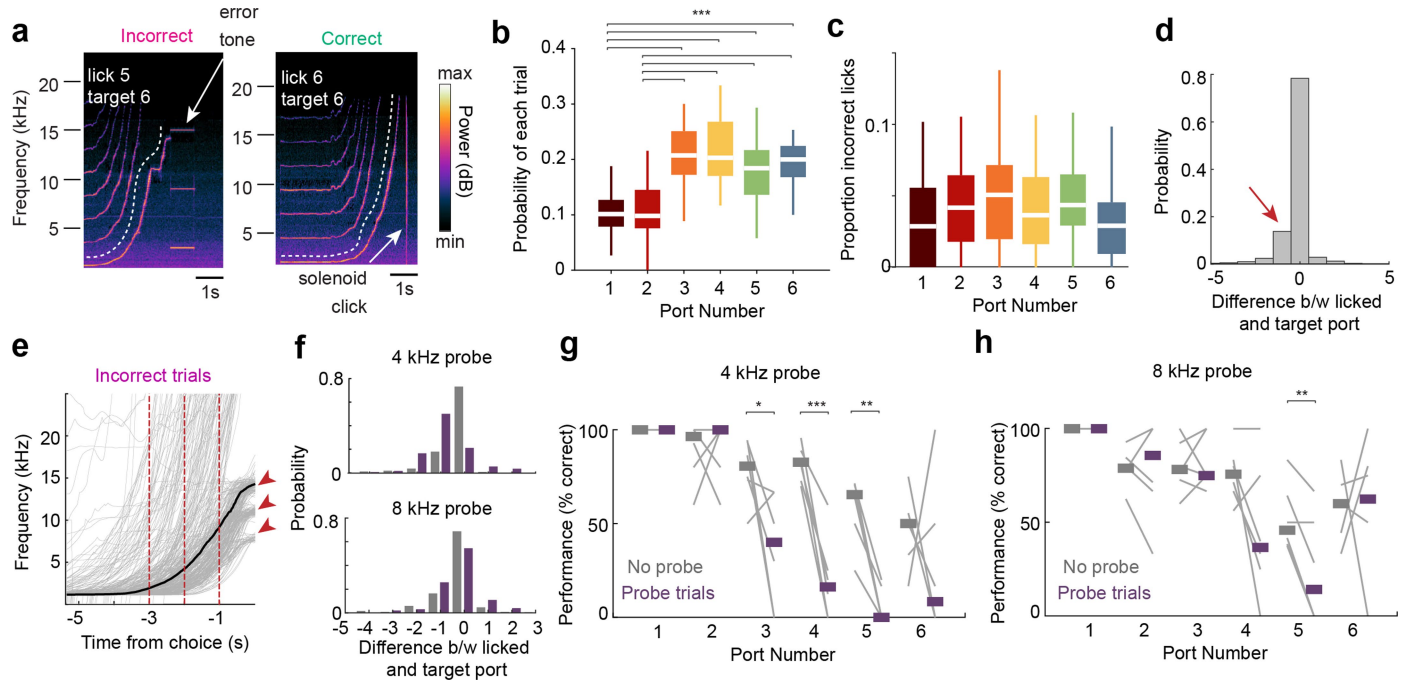
Supplementary information The online version contains supplementary material available at <https://doi.org/10.1038/s41586-024-08397-7>.

Correspondence and requests for materials should be addressed to György Buzsáki.

Peer review information *Nature* thanks Clifford Kentros and the other, anonymous, reviewer(s) for their contribution to the peer review of this work.

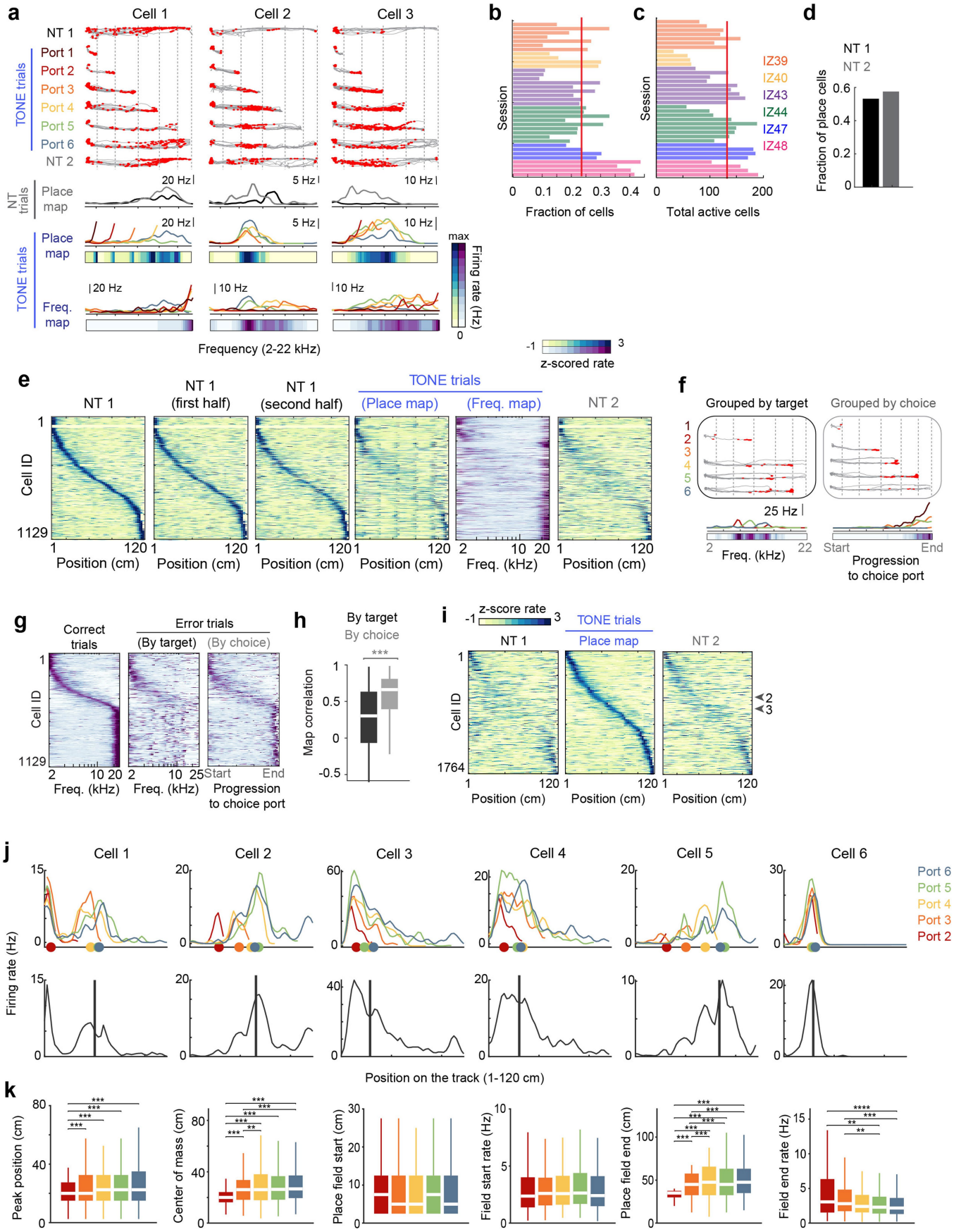
Reprints and permissions information is available at <http://www.nature.com/reprints>.

Article



Extended Data Fig. 1 | Behavioral variability for ports 1–6. (a) Spectrogram of frequencies recorded in an incorrect and correct trial. Power below the white dashed lines represents the tones playing, while the power bands above the white lines correspond to analytical harmonics. A 3 kHz tone was played for 1 s after mice made an erroneous lick (*left*; error tone), with no water delivery. Mice received a water reward if they poked at the correct port (*right*, white arrow, solenoid delivery made a clicking sound). (b) The probability of trials was deliberately unevenly distributed to yield more trials where mice performed longer runs on the track. Thus, the first two ports were less frequently rewarded than the later ones (Friedman followed by Tukey-Kramer two-sided post-hoc tests, Chi-square (5,180) = 61.47, $p = 6.02 \times 10^{-12}$). (c) The fraction of times the mouse incorrectly poked at a specific port compared to all trials where that port was not the target ($n = 37$ sessions from 6 mice, Friedman test, Chi-sq (5, 180) = 9.50, $p = 0.0906$). (d) Histogram of the difference between the target and choice port. Most errors occurred when mice licked one port sooner than the target (red arrow). (e) Tone frequency progression of each trial (gray lines) in time, superimposed with the average frequency (black) for incorrect trials across all mice and sessions. If the mice overshot the target, the tone was cut off

beyond 25 kHz. The discrete branches (red arrowheads) reflect errors one (*top*), two (*middle*), or three ports (*bottom*) before the target. Red lines are at -3, -2, and -1 s before the first lick. Compare with Fig. 1f. (f) Histogram of the difference between the choice and the target port for regular (“no probe”; gray) and probe (purple) trials. During 4 kHz trials, the mice generally made errors by licking earlier (“undershooting”), while during 8 kHz trials, the mice made both undershooting and overshooting errors. (g) Behavior performance during 4 kHz probe trials for each port. Impairment was only observed for ports 3–5. For port 6, the effect was variable, possibly because mice would interpret the truncation of the tone to signal a NT trial and run straight to port 6 (Two-sided paired t-test, $n = 6$ sessions from 2 mice, Port 1: $p \approx 1$; Port 2: $p = 0.92$, Port 3: $p = 0.044$; Port 4: $p = 8.38 \times 10^{-4}$, Port 5: $p = 0.0012$; Port 6: $p = 0.67$). (h) Same as (g) but for 8 kHz probe trials. An impairment was observed for both Port 4 and Port 5, but only Port 5 reached significance (Two-sided paired t-test, $n = 6$ sessions from 2 mice, Port 1: $p \approx 1$; Port 2: $p = 0.94$, Port 3: $p = 0.82$; Port 4: $p = 0.09$, Port 5: $p = 0.0084$; Port 6: $p = 0.76$). * $p < 0.05$, ** $p < 0.01$, *** $p < 0.001$. All box plots show median \pm interquartile; whiskers show range excluding outliers. Lines in g–h show median.

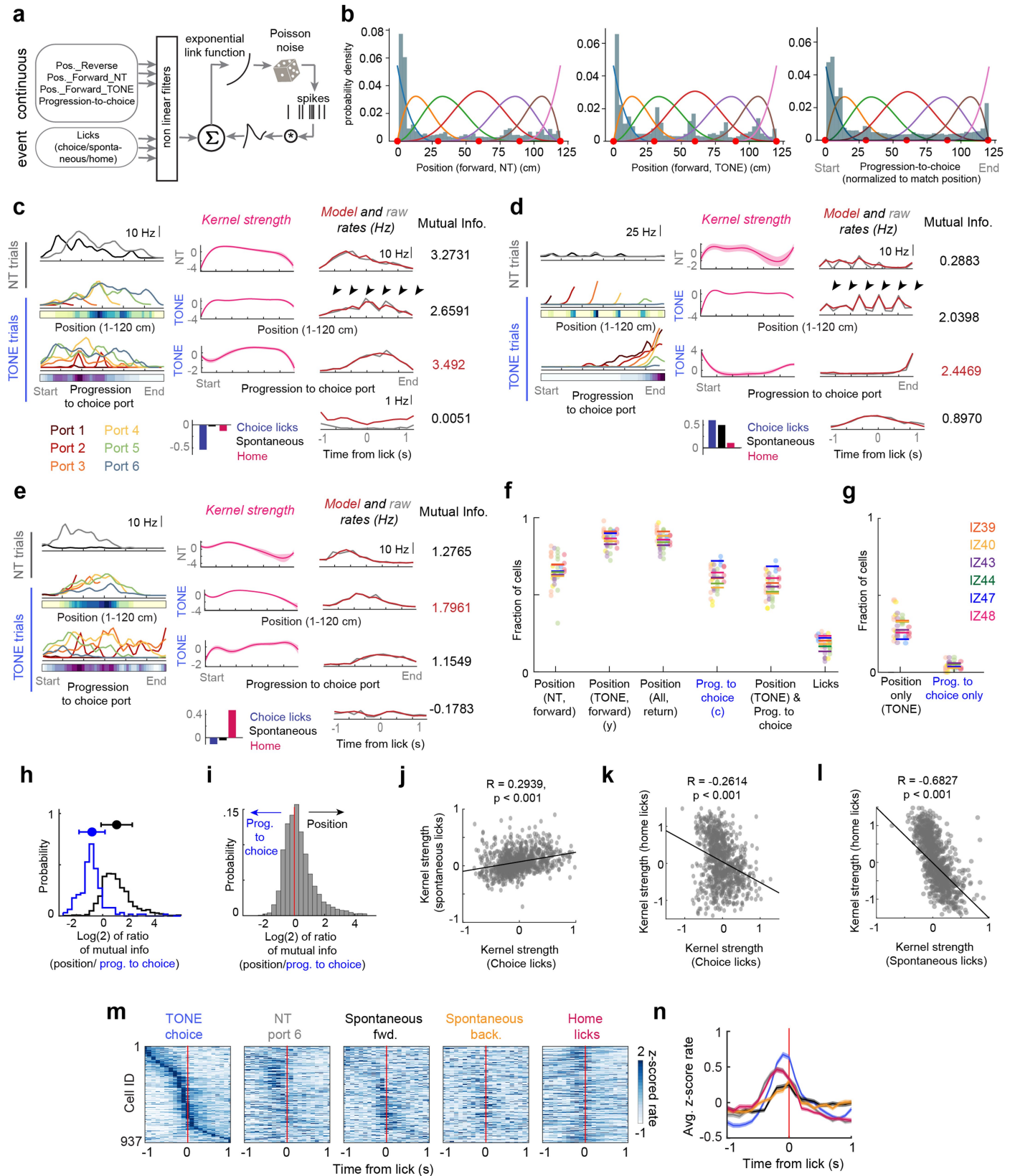


Extended Data Fig. 2 | See next page for caption.

Article

Extended Data Fig. 2 | Modulation of hippocampal cells by space and approach to ports. (a) Additional examples of CA1 pyramidal cell firing. See Fig. 2a for a detailed description. (b) Fraction of pyramidal cells responding to the “tone” varied for each session (*bars*) and animal (*colors as in (c)*). *Red line*, median. The successive color bars in each mouse correspond to subsequent sessions (*top*, earliest recorded session). (c) Total number of active pyramidal cells (average firing rate > 0.2 Hz) recorded in each session of (b). *Red line*, median. The successive color bars in each mouse correspond to subsequent sessions (*top*, earliest recorded session). (d) A substantial fraction of tone cells had a definable place field in the NT trials, suggesting that tone cells are not a unique class. (e) Same “tone cell” population as in Fig. 2b, but sorted according to spatial position preference during NT1 trials. Dividing NT1 trials into halves revealed stable place fields during NT1, but mainly non-spatial firing during TONE trials. Thus, tone cells could be spatially tuned on the same track depending on the context. Sorting was maintained across display conditions. (f) Example firing of a tone cell on error trials. The average rate maps were generated by grouping trials by the target port (correct) or mouse’s choice port (incorrect). Thus, these average maps corresponded to the auditory frequency (*left*, tuning to sensory variable) or the progression to the choice port (*right*, tuning to movement trajectory). The average ‘choice maps’ were calculated by scaling the trajectories to the mouse’s chosen port, reflecting the normalized distance to the choice (*progression-to-choice, 0-1 or start-end*). (g) The average firing of tone cells in error trials, sorted as during correct trials. Averaging by the choice of the mouse, but not the target, more closely matched the firing of the same cells during correct trials. Thus, sound-induced firing reflects the movement trajectory to the choice port rather than responding to sensory variables. Colormap as in (e). (h) Cell-by-cell correlation of tone cells with their

frequency maps during correct trials, versus during error trials, grouped by target (*g, left*) or choice (*g, right*) ($n = 1129$ cells from 37 sessions in 6 mice, Wilcoxon two-sided paired signed rank test, $z = -18.96, p = 3.47 \times 10^{-80}$). (i) All cells with a significant firing field during TONE trials in the place map (averaged across Ports 1–6) are ordered by spatial preference. Spatial tuning persisted but was significantly altered between NT1 and TONE trials (see Extended Data Figs. 6 and 7). Cells 2 & 3 from *a* are highlighted on the *right*. (j) Six example cells with a defined place field across all tone trials. *Bottom*, average rate map across all trials, *vertical black line*, center of mass of rate map. *Top*, colored lines, rate maps of the cell after separating trials by approach to ports 1–6. Colored dots, center of mass of each rate map. A variety of effects were observed, ranging from shifting place fields (Cell 1, 2), expanding place field tails (Cells 3, 4), truncating place fields (Cell 5), and stable fields (Cell 6). (k) Group statistics comparing port-specific rate maps of place cells. To ensure a fair comparison across all ports, cells must have a stable field in each port-specific rate map (Ports 2–6) within 30 cm of the averaged field (*black line inj*). There was a significant effect of place field peak and the center of mass shifting (e.g., Cell 1, 2), place field tails expanding (e.g., Cell 3, 4), and place field rates at the end of the field decreasing, suggesting truncation (e.g., Cell 5). (Friedman test followed by two-sided Tukey-Kramer post-hoc tests, $n = 321$ cells, peak position: Chi-sq (4,1280) = 60.66, $p = 2.1 \times 10^{-12}$; center of mass: Chi-sq (4,1280) = 199.46 $p = 4.91 \times 10^{-42}$; start of place field: Chi-sq (4,1280) = 2.47, $p = 0.65$; place field start rate: Chi-sq (4,1280) = 7.91, $p = 0.095$; end of place field: Chi-sq (4,1280) = 353.68, $p = 2.81 \times 10^{-75}$; place field end rate: Chi-sq (4,1280) = 34.23, $p = 6.69 \times 10^{-7}$). ** $p < 0.01$, *** $p < 0.001$. All box plots show median \pm interquartile; whiskers show range excluding outliers.

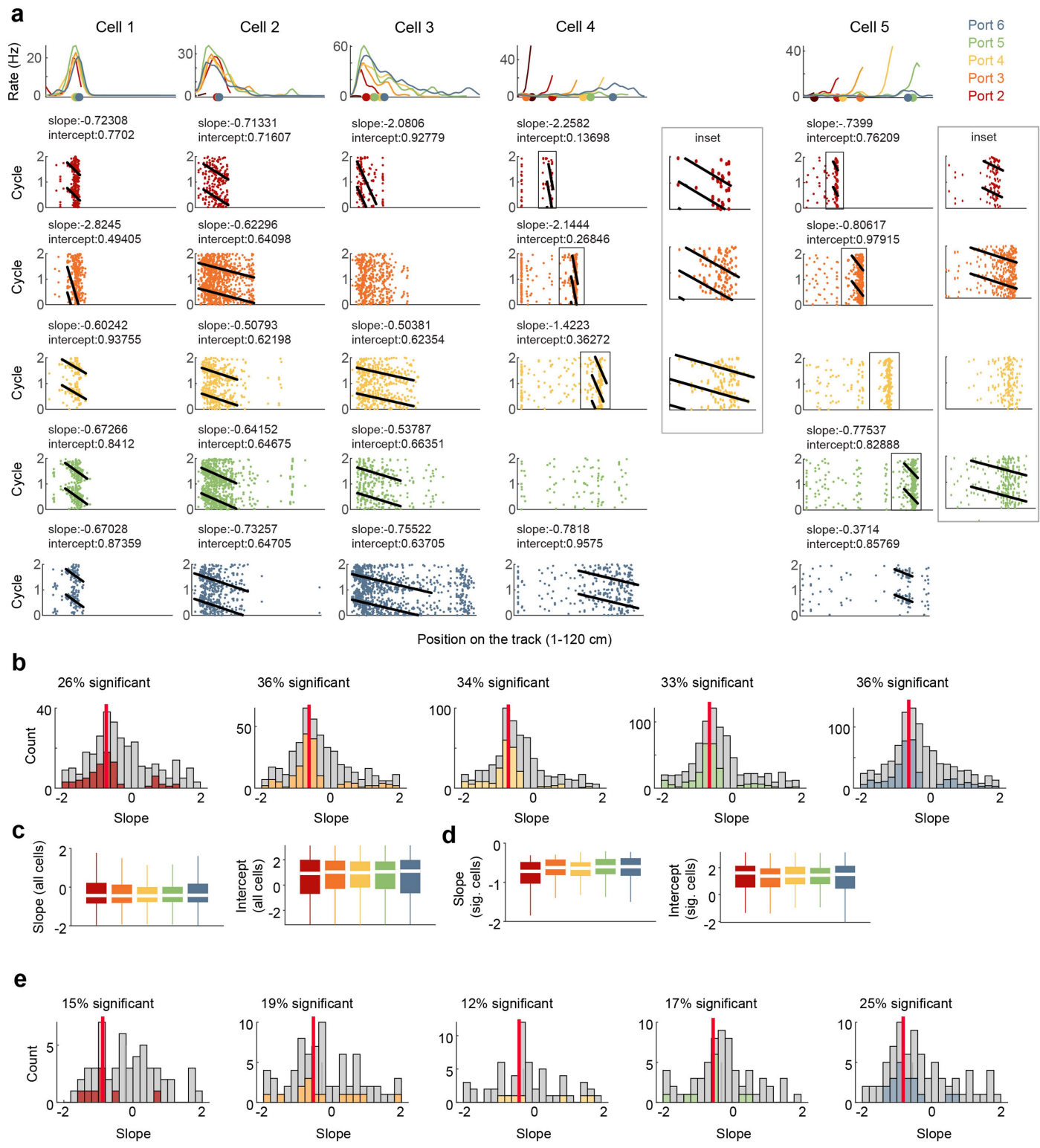


Extended Data Fig. 3 | See next page for caption.

Article

Extended Data Fig. 3 | Fitting multiple behavior variables to model single-cell firing. (a) Schematic of the Poisson generalized additive model (P-GAM) used to fit spike trains. Inputs to the model included continuous task variables such as the position in NT and TONE trials for the forward and reverse runs and the progression-to-choice for the forward TONE trials. Event variables included all detected lick epochs, i.e., the first lick at a port visit. Subsequent licks within a visit were not included. Licks were grouped into choice during TONE trials, port 6 during NT trials, spontaneous and home port licks (see Fig. 3i–k), and a step kernel function was fit for each lick type (see Methods). (b) Distribution of the continuous input variables for an example session. Knots (*red circles*) were defined to sample the distribution equally and B-splines (*colored lines*) for the P-GAM were constructed based on these knots. (c–e) Three example neurons, modeled using the P-GAM. *Left*, average rate maps constructed from the spike trains for each continuous variable. *Middle*, Kernel strength (β), that, when convolved with the B-splines, generated the best fit of the neuron's tuning curve. The kernel strength for the step function of each type of licks is shown as bars on the bottom plot. *Right*, True tuning curve (gray), and the tuning curve generated by the reduced model (*red*; i.e., only those variables that were significantly contributing to the firing of the neuron). *Right*, mutual information (MI) between the firing of the cell and each continuous variable. The highest MI for each cell is shown in *red*. The fit for licks was non-significant for the neuron in (c), but all other fits were classified as significant. (f) Fraction of neurons tuned to each variable across mice (*colored lines*) and sessions per mouse (*colored dots*). A large fraction of neurons (>50%) were significantly modulated by both position and progression-to-choice. (g) Fraction of neurons tuned only to position in TONE trials or to progression-to-choice. (h) The MI of cells tuned only to position (*black*), or progression-to-choice (*blue*) as shown in (g). The MI for each group was ~ two-fold higher for the significant variable

($n = 1197$ cells tuned to position, 189 cells tuned to progression-to-choice, mean \pm standard deviation). (i) The distribution of the ratio of the MI for position versus progression-to-choice by only selecting cells significantly modulated by both variables. The distribution was centered around 0, with a larger skew towards spatial position. (j) Scatter of the kernel strength of choice licks during TONE trials, versus spontaneous licks for all cells significantly tuned to licks. The significant correlation confirms that cells were co-modulated by spontaneous and choice licks, thus irrespective of whether mice were performing the task and whether the water reward was present (Pearson's correlation, $n = 937$ cells, $R = 0.2939, p = 3.99 \times 10^{-20}$). (k, l) Same as (j), but for choice versus home (Pearson's correlation, $n = 937$ cells, $R = -0.2614, p = 4.24 \times 10^{16}$), and spontaneous versus home licks (Pearson's correlation, $n = 937$ cells, $R = -0.6827, p = 1.533 \times 10^{-129}$). A significant decorrelation was observed, confirming that cells tuned to choice or spontaneous licks did not fire during the home port licks. Note the negative correlation between choice lick and home port lick-related firing even though both port types yielded the same amount of water reward, again indicating that the presence or absence of water reward *per se* was not a critical variable in determining neuronal firing patterns. (m) PSTH of all cells significantly tuned to licks using the PGAM. Unlike Extended Data Fig. 9d, which selectively examined tone cells, this analysis identified cells that were tuned to any lick during the session. Separating their firing into distinct lick types shows distinct groups firing to the NT, Home, and TONE choice licks. Note the peak firing still occurs before the first detected lick. (n) Average PSTH of all cell groups shown in (m). Colors indicate lick types as in (m). The shifted and broader peak of NT and Homeport licks reflects a different type of lick response compared to the tone choice licks and could emerge from place cells with a field at the ends of the track. Lines are mean \pm sem.

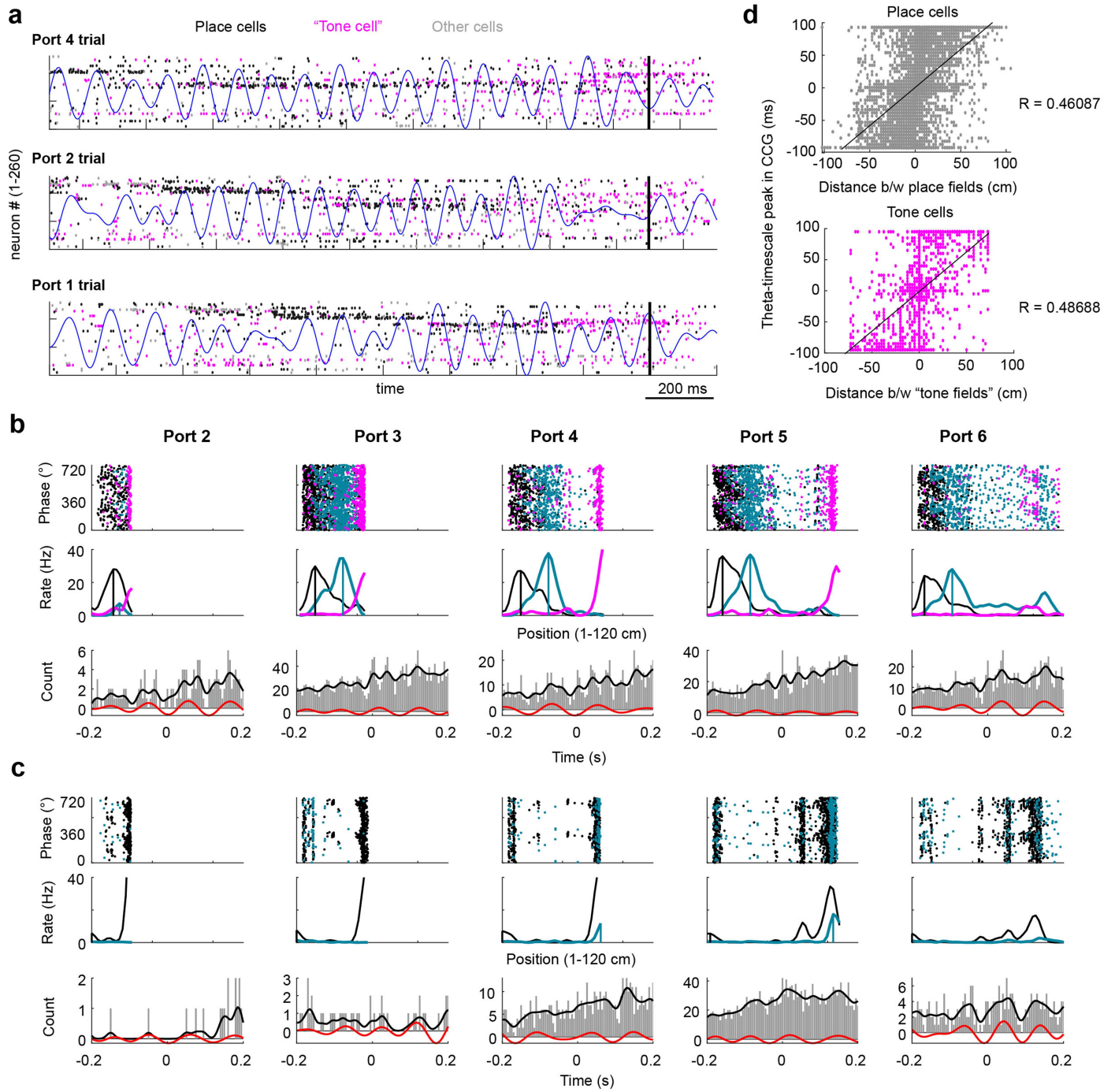


Extended Data Fig. 4 | See next page for caption.

Article

Extended Data Fig. 4 | Phase precession of place and tone cells by approach to each port. (a) *Top row*, Five example cells across different sessions showing average ratemaps of the cell for each port. Cells 1–3, “place cells”. Cells 4–5, tone cells. *Colored dots on x-axis*, center of mass. *Rows 2–6*, theta phase by position plots for each cell, separated by trials to ports 2–6. For the tone cells, slopes were difficult to observe because of their small fields. Yet, clear examples of phase precession also occurred (see inset of ports 2–5 for Cells 4 and 5). The slope was calculated by identifying field boundaries for each port and scaling the place field size between 0 and 1. (b) *Left to right*, Distribution of phase precession slopes across ports 2–6 for place cells. *Gray bars*, all slopes. *Colored bars*, significant slopes. Colors as in (a). Fraction of significant slopes compared to all slopes is provided for each condition. *Red line*, median of significant slopes. (c) *Left*, Average phase precession slope of all place cells across port approaches. *Right*, Average phase precession intercept of all cells across port approaches. Colors as in (a). No effect was observed ($n = 306\text{--}952$

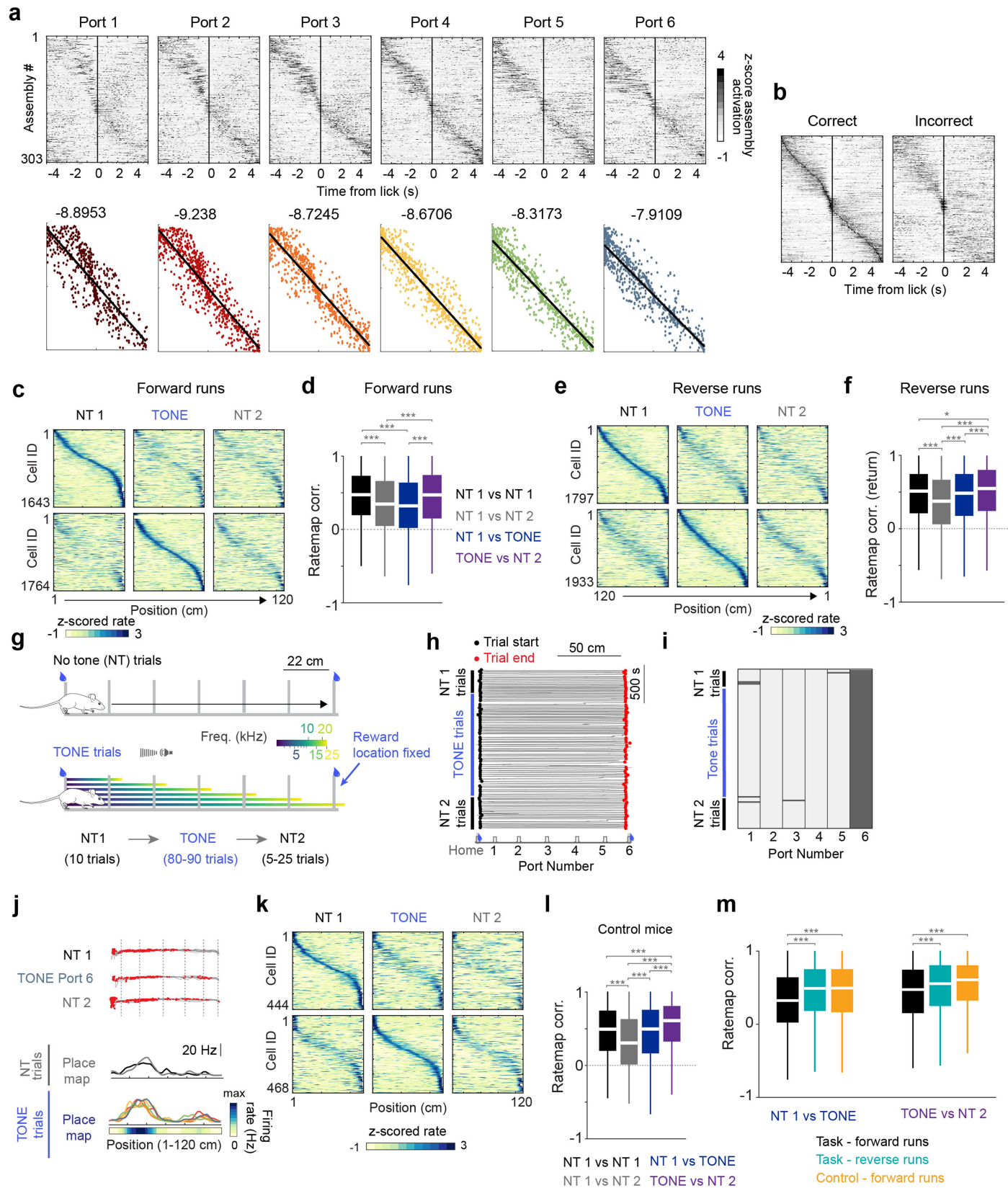
cells, Kruskal Wallis test followed by Tukey-Kramer two-sided post-hoc tests. Slope: Chi-sq (4,3097) = 1.42, $p = 0.84$; Intercept: Chi-sq (4,3097) = 0.55, $p = 0.97$. (d) *Left*, Average phase precession slopes of place cells with significant slopes across port approaches. *Right*, average intercept of significantly fit slopes ($n = 80\text{--}344$ cells, Kruskal Wallis test followed by Tukey-Kramer two-sided post-hoc tests. Slope: Chi-sq (4,1048) = 10.69, $p = 0.03$; Intercept: Chi-sq (4,1048) = 1.56, $p = 0.82$). Because the slope was calculated by normalizing place field size, no change in the slope implies that expanding fields would have spikes occurring in earlier theta phases at the same location compared to smaller fields (e.g., compare Port 2 and Port 6 trials of Cell 2 in (a). Despite similar slopes, the expanding field for Port 6 leads to a different theta phase of spikes). Colors as in (a). (e) Same as (b), but for tone cells. A smaller fraction of cells had significant slopes, possibly because of the smaller fields. Colors as in (a). All box plots show median \pm interquartile; whiskers show range excluding outliers.



Extended Data Fig. 5 | Theta sequences observed for both place and tone cells. (a) Spike rasters of three example trials from an example session (see Fig. 4). All active pyramidal cells are shown sorted using Rastermap (see Methods). Black dots, spikes from place cells, pink dots, spikes from tone cells, gray dots, spikes from non-classified cells. Black vertical line indicates time of first lick. Blue trace, filtered local field potential in the theta (6–12 Hz) band. Note that place cell sequences precede “tone cell” firing that ramps in the 0.5 s preceding the lick. Note also that “tone cell” spikes are interleaved with place cell spikes and begin -1 s before the lick. (b) Top, theta phase-of-spike by position plots for three example cells. Blue and black, place cells,

pink, “tone cell”. Middle, Firing rate maps of each cell. Vertical lines, peak of the place fields. Bottom, Cross-correlogram (CCG) between the black and blue cells. Red line, filtered trace of the cross-correlogram in the theta-band. (c) Same as (b), but for two tone cells. (d) Distance to time compression. Top, scatter plot of the distance between place field peaks and the time lag in the CCG between cell pairs. Bottom, same as above but for tone cells. Distance between tone fields was calculated in the progression-to-choice domain. Both correlations were significant (Pearson correlation, Place cells: $n = 5771$ cell pairs, $R = 0.4609, 1.8 \times 10^{-301}$; Tone cells: $n = 2474$ cell pairs, $R = 0.4869, p = 1.9 \times 10^{-147}$).

Article

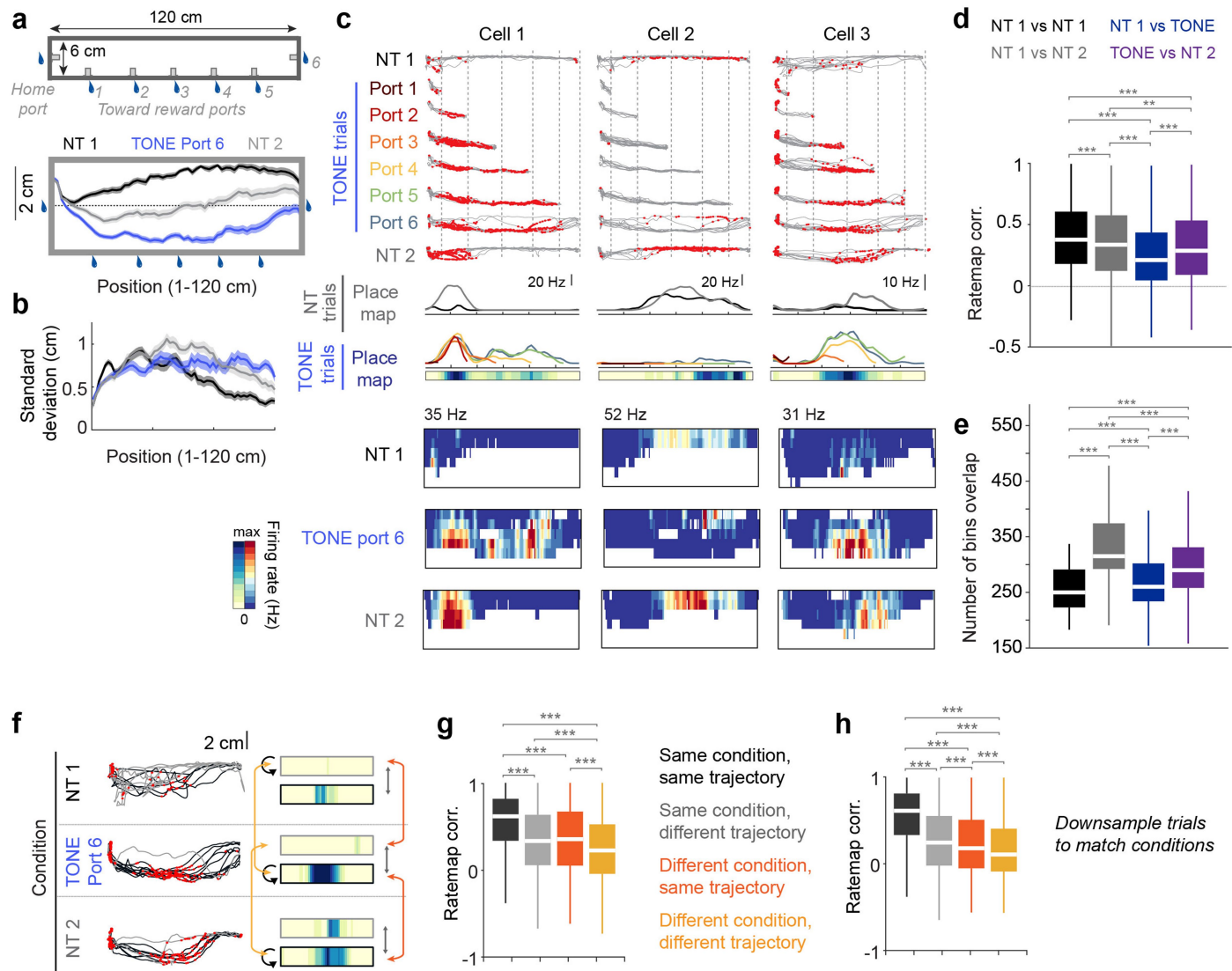


Extended Data Fig. 6 | See next page for caption.

Extended Data Fig. 6 | Evolution of cell assemblies and controls for spatial remapping. (a) Cell assemblies across all sessions were detected using ICA (see Methods). Their activation around the end of the trial (i.e., lick at the chosen port) was calculated, separated by ports 1–6. *Top*, Assemblies were sorted by their activation profile calculated across all trials (see left plot in (b)) and the sorting order was maintained for the port-wise peri-event time histograms (PETH). The temporal width of the sequence expands from Ports 1–6. *Bottom*, Peak latency for each assembly as shown above. Sorting is maintained for Ports 1–6. *Lines and titles* show the regression slope decreasing from Ports 1–6. (b) Cell assembly PETH for the time of all correct choice licks. The same assembly sorting is maintained for error trial licks. Note similar cell assembly sequences in both correct and error trials in the 1 s leading up to the lick. (c) Average firing rate maps for NT1, NT2 and TONE port 6 trials (to control for path length). *Top*, Cells with a detected place field (for place field definition, see Methods) in NT1 trials, sorted by their preferred location. *Bottom*, Same as above, but for cells with a place field during TONE trials. (d) Statistics for cell-by-cell correlations in (c) ($n = 3004, 2767, 2869, 2618$ cell-cell pairs; Kruskal Wallis test followed by Tukey-Kramer two-sided post-hoc tests, Chi-sq (3,11254) = 242.62, $p = 2.58 \times 10^{-52}$). (e) Same as (c) but for place fields on the return runs. (f) Same as (d) but for place cells on the return runs. There was a general drift in the spatial map, but no significant remapping between NT1 and TONE trial return runs ($n = 2824, 2582, 2697, 2450$ cell-cell pairs; Kruskal Wallis test followed by Tukey-Kramer two-sided post-hoc tests, Chi-sq (3,10549) = 199.99, $p = 4.22 \times 10^{-43}$; NT1 vs NT1 and NT1 and TONE Port 6, $p = 0.304$). (g) To control for the presence of the sensory cue, we trained a separate cohort of mice ($n = 3$) on a similar task. NT and closed-loop TONE trials alternated as in the main task, but rewards were always provided only at the two ends of the track. Thus, the tone had no significance. Tones would stop playing after 25 kHz. The mouse schematics in panel g were created using SciDraw (<https://scidraw.io>)

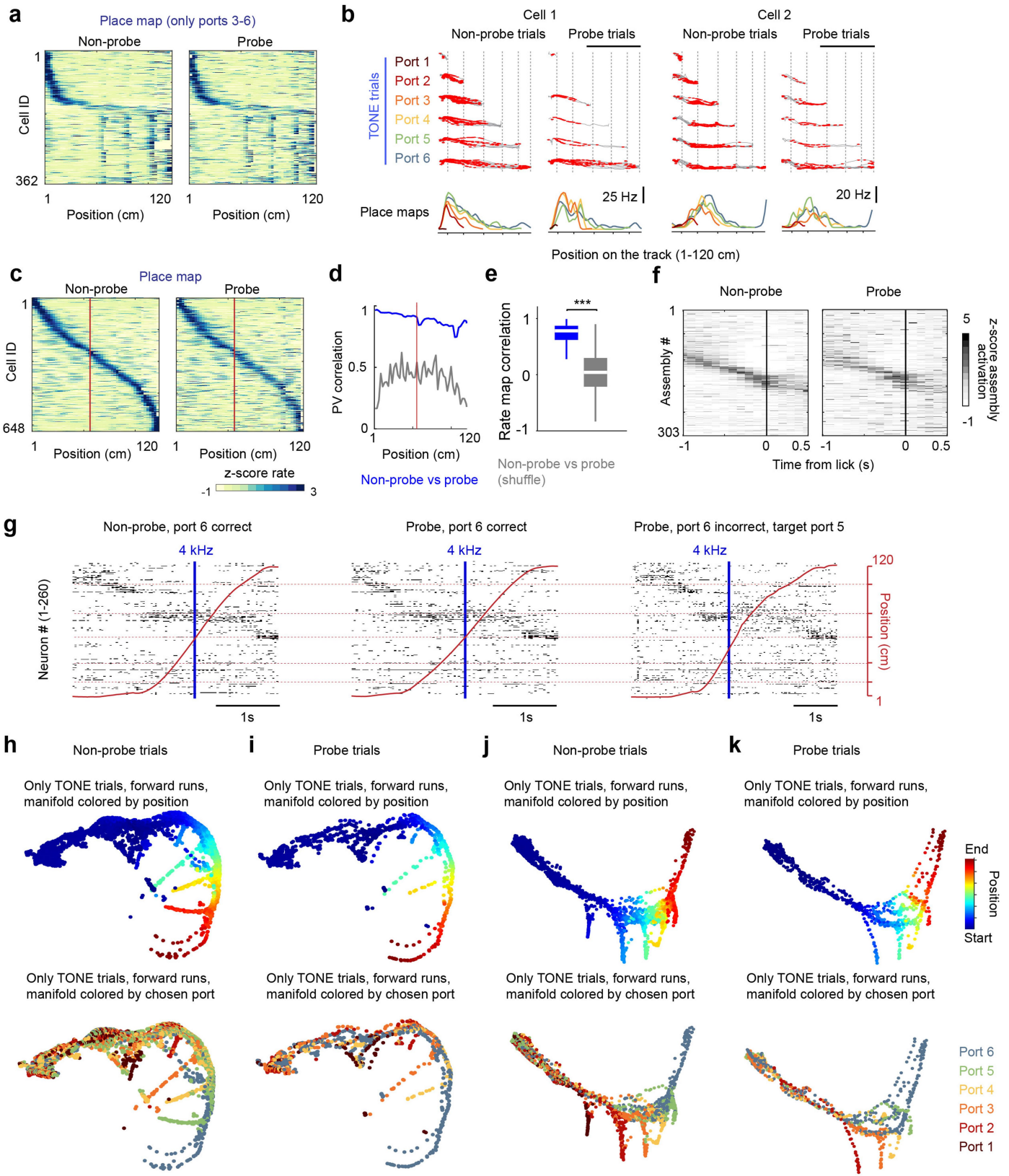
under a Creative Commons licence CC BY 4.0 (credit E. Tyler and L. Kravitz)⁵¹. (h) Trajectory of a mouse from an example control session. (i) Heatmap showing licks detected at each port (*dark gray*) from the session in (h). (j) Example CA1 pyramidal cell recorded from a mouse trained on the control task. *Top*, Trajectories (*gray lines*) separated by NT1, TONE Port 6 and NT2. Spikes from a single neuron are overlaid in *red*. *Bottom*, Average spatial firing rates are shown for each trial type – NT1, individual TONE trials, NT2. *Rainbow shades*, TONE trial types 1–6. (k) Average rate maps from control mice for NT1, NT2 and port 6 TONE trials (to match the analysis performed for the auditory task mice, see (c)). *Top*, Cells with a detected place field in NT1 trials, sorted by their preferred location. *Bottom*, Same as above, but for cells with a place field during TONE trials. (l) Statistics for cell-by-cell correlations in (k). The results mirror the effect observed for the return runs in the auditory task mice, i.e., a general drift of the map led to a decorrelation between NT1 and NT2 trials (*gray*), but no significant remapping was observed between NT1 and TONE trials (*blue*) ($n = 749, 674, 756, 676$ cell-cell pairs; Kruskal Wallis test followed by Tukey-Kramer two-sided post-hoc tests, Chi-sq (3,2851) = 114.60, $p = 1.12 \times 10^{-24}$; NT1 vs NT1 and NT1 and TONE Port 6, $p = 0.974$). (m) Comparison of the three conditions that are separated by similar time lags but show different magnitudes of remapping. Only the TONE forward runs led to remapping between NT and TONE trials, suggesting a significant role of task engagement that cannot be explained by changes in sensory inputs or representational drift (NT1 vs TONE, $n = 2869, 2697, 756$ cell-cell pairs; Kruskal Wallis test followed by Tukey-Kramer two-sided post-hoc tests, Chi-sq (2, 6319) = 174.49, $p = 1.28 \times 10^{-38}$; TONE vs NT2, $n = 2618, 2450, 676$ cell-cell pairs; Kruskal Wallis test followed by Tukey-Kramer two-sided post-hoc tests, Chi-sq (2, 5741) = 55.03, $p = 1.12 \times 10^{-12}$). * $p < 0.05$, *** $p < 0.001$. All box plots show median ± interquartile; whiskers show range excluding outliers.

Article



Extended Data Fig. 7 | Spatial remapping depends on the mouse’s running trajectory. (a) Top, top-view schematic of the track showing the wall with the middle reward ports. Bottom, Movement trajectory ($\text{mean} \pm \text{sem}$) across all mice for NT1 (black), TONE port 6 (blue) and NT2 trials (gray). The length and width ratios are distorted to emphasize small wall-guided deviation from a straight line on the track (dashed thin line). Note how mice avoided the port wall in NT1 trials, ran along the port wall in TONE trials, and midway between the two during NT2 trials. (b) Average standard deviation of the trajectory of the mouse along the width of the track. Trajectories were more variable for NT2, and TONE trials compared to NT1. Colors as in (a). (c) Top, three example cells with a place field recorded as mice ran with varying movement trajectories during NT1, TONE port 6 and NT2 trials. The firing of these cells was modulated by movement trajectory. Middle, one-dimensional linear maps for NT and TONE trials. Bottom, two-dimensional maps constructed for the same cells using 1 cm wide bins along the width of the track. Areas with no occupancy are shown in white. (d) Cell-by-cell correlation of the two-dimensional maps shown in (c). The decorrelation between NT1 and TONE trials persisted despite using a two-dimensional map ($n = 1798, 1117, 2035, 2211$ cell-cell pairs; Kruskal Wallis test followed by Tukey-Kramer two-sided post-hoc tests, Chi-sq (3,7157) = 256.57, $p = 2.48 \times 10^{-55}$). Only overlapping bins were considered for the correlation. (e) Average number of bins included for each correlation in (d). While the bin numbers were different, the trends did not match that of (d), suggesting the effect was not driven by the number of bins (Kruskal Wallis test followed by Tukey-Kramer two-sided post-hoc tests, Chi-sq (3,7163) = 1196.1, $p = 5.27 \times 10^{-259}$).

(f) Left, spikes from an example cell (red dots) overlaid with the mouse’s trajectories during NT1, TONE port 6 and NT2 trials. Trajectories were clustered according to their distance from the top wall of the track (gray versus black lines; see Methods). It was possible to have all trajectories within a condition to be of a particular cluster. Right, Rate maps were calculated independently for gray and black trajectories during NT1, TONE port 6, and NT2 trials (box color outlining the rate maps). Correlations between these rate maps were performed as depicted by the colored arrows. (g) Average cell by-cell rate map correlations separated by different conditions (NT1, TONE Port 6, NT2) and trajectory (gray/black) comparisons as shown in (f). Black, within condition, the same trajectory was used as a baseline. Gray, changing trajectories even within the same condition altered the spatial map. Orange, the same trajectory, but different conditions also led to remapping. Yellow, there was an additive effect of trajectory and condition, suggesting both features combine to impact spatial firing ($n = 5706, 4680, 10618, 10491$ cell-cell pairs after pooling across similar groups; Kruskal Wallis test followed by Tukey-Kramer two-sided post-hoc tests, Chi-sq (3,31491) = 2425.1, $p = 0$). (h) Same as (g), but rate maps were downsampled to match the number of black and gray trajectories. Only conditions that had at least one of each trajectory type were compared ($n = 5706, 4601, 3366, 3362$ cell-cell pairs after pooling across similar groups; Kruskal Wallis test followed by Tukey-Kramer two-sided post-hoc tests, Chi-sq (3,17034) = 2796.3, $p = 0$). Note that remapping occurred between NT and TONE trials even when the trajectories were the same. ** $p < 0.01$, *** $p < 0.001$. All box plots show median \pm interquartile; whiskers show range excluding outliers.

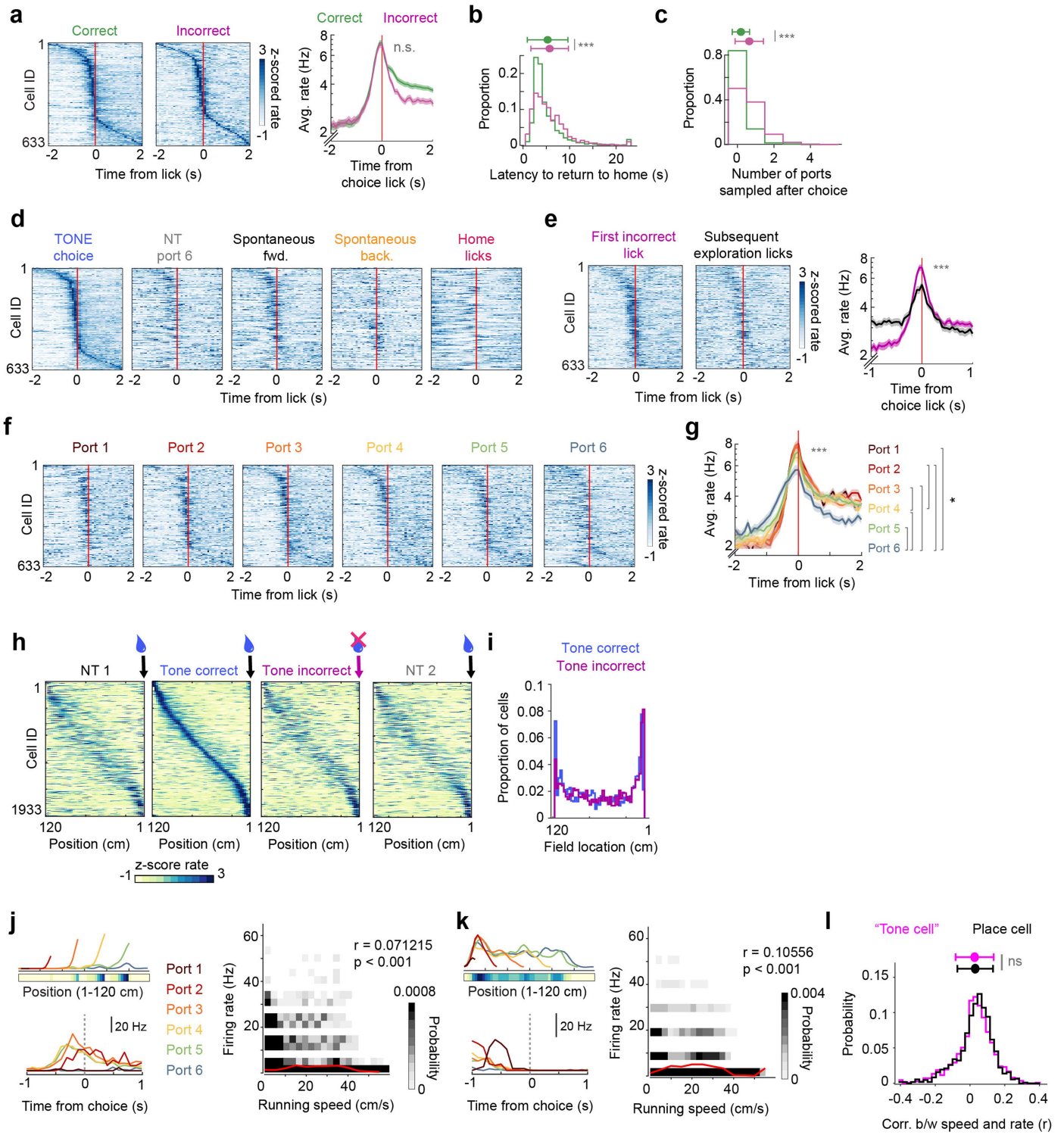


Extended Data Fig. 8 | See next page for caption.

Article

Extended Data Fig. 8 | Similar evolution of cell assemblies during non-probe and probe trials. (a) Spatial maps of tone cells during non-probe and probe trials (sorted as Fig. 3b). Because no behavioral impairment was observed for ports 1–2 (Extended Data Fig. 1g), probe trials were only performed for ports 3–6 as targets. (b) Rate maps of two example place fields separated by port trajectory for probe and non-probe trials. A similar modulation of place fields by approach to the reward (Extended Data Fig. 2j) was also observed for probe trials. (c) Firing rate maps of all place cells detected using TONE Port 6 trials. The cells were sorted by their place field preference during non-probe trials and the same sorting was maintained for probe trials. Red line indicates position where tones were truncated during probe trials. Truncation of the tone did not affect the spatial map. (d) Population vector (PV) correlation for the heatmaps in panel c (blue line) compared to shuffled data (gray). The red line indicates the position where tones stopped during probe trials (as in c). (e) Cell-by-cell rate map correlations for the place cells in (c) (blue) compared to shuffled data (gray). Only cells with a place field after the red line, i.e., after the tones stopped playing during probe trials, were included in the analysis. Place maps remained stable, indicating that the removal of the tone did not impact the spatial map ($n = 395$ cells from 8 sessions in 2 mice, Wilcoxon two-sided rank sum test against shuffled data, $z = 29.66, p = 2.63 \times 10^{-193}$). (f) Cell assemblies

across all sessions were detected using ICA (see Methods) and their activation around the end of the trial (i.e., lick at the chosen port) was calculated. Cells are sorted by their latency in non-probe trials, and the sorting is maintained for probe trials. A stable cell assembly sequence persisted during probe trials, particularly in the -1 s preceding the lick. (g) Spikes sorted by rastermap (see Methods) for the same session as Fig. 4c. Three port 6 trials are shown: one non-probe (left), one probe correct (middle), and one probe incorrect (right). Red line is the mouse's spatial position and blue line indicates the time when the tone was truncated (middle and right) or when the tone was playing at the probe frequency (left). Red horizontal dashed lines, port locations. Similar evolution of spiking activity was observed across all conditions. (h) Neural manifold generated using UMAP (see Fig. 4 and Extended Data Figs. 11–13) showing non-probe TONE trials in an example session. Dots are individual time bins colored by position (top), or by trials according to the chosen lick port (bottom). (i) Same session as in (h), but for probe trials. The manifold shape is maintained, supporting the analysis that truncation of tones did not impact cell assembly sequences. Note no Port 5 probe trials occurred in this session. (j–k) Same as (h–i), but from a different animal. *** $p < 0.001$. All box plots show median \pm interquartile; whiskers show range excluding outliers.

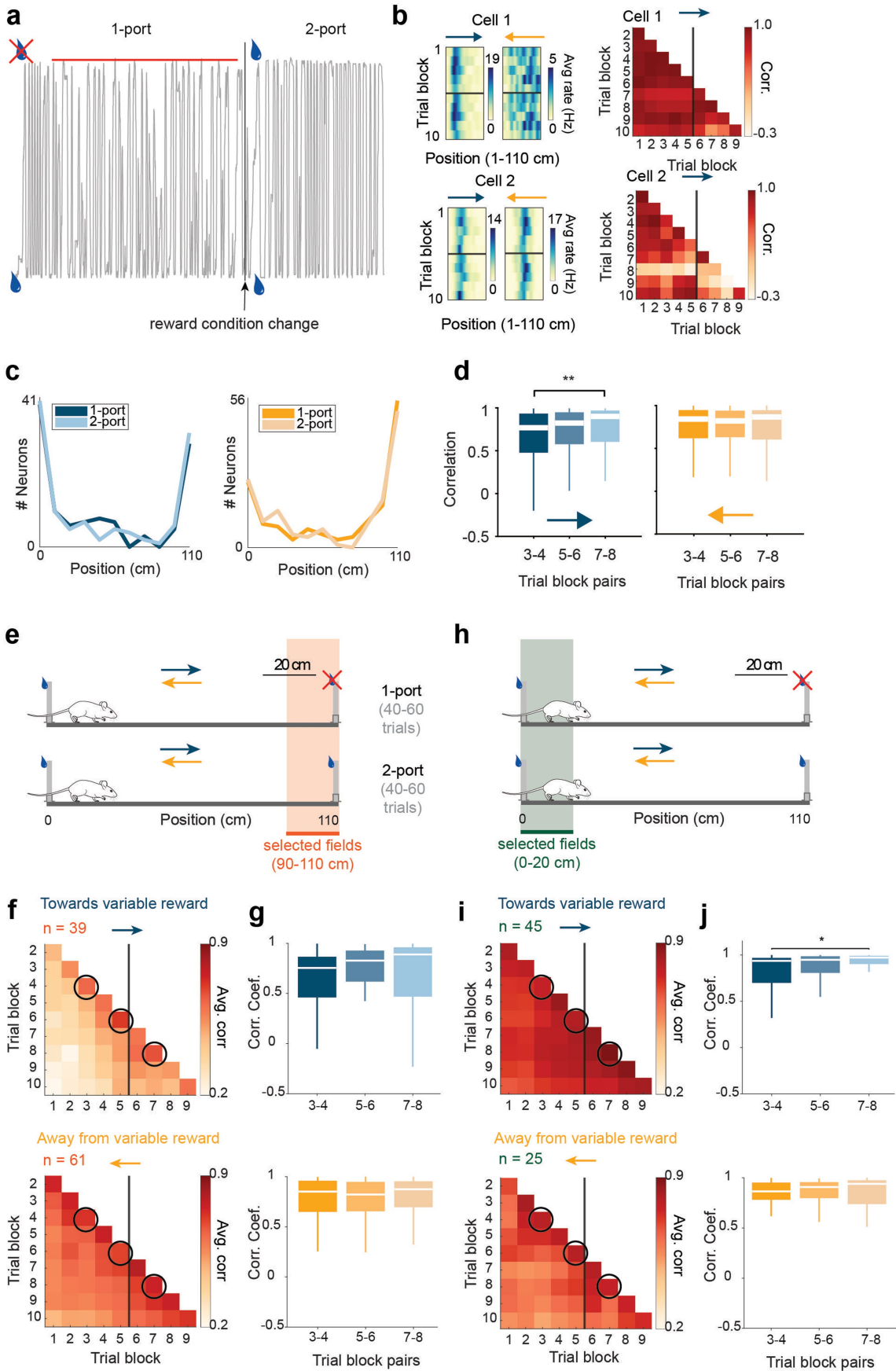


Extended Data Fig. 9 | See next page for caption.

Article

Extended Data Fig. 9 | Tone cells were not directly modulated by reward or running speed. (a) *Left*, Peri-stimulus time histogram (PSTH) of tone cells for all choice licks during TONE trials, separated by correct (*rewarded*) and incorrect (*unrewarded error trial*) licks. To specifically examine the response to rewards, only tone cells firing at the target frequency 18–22 kHz have been included. Cells are sorted by their latency in the TONE correct trials and the sorting is maintained. 0 s = first lick. *Right*, Average PSTH across tone cells for correct and incorrect licks. No significant difference was observed between the two ($n = 633$ reward-related tone cells, Wilcoxon two-sided signed rank test, $z = 1.03, p = 0.30$). (b) The latency to return to the home port after an incorrect lick was significantly higher than after a correct lick ($n = 2079$ vs 791 trials, Wilcoxon two-sided rank sum test, $Z = -4.55, p = 5.47 \times 10^{-6}$). (c) The number of ports sampled before returning to the home port after an incorrect lick was higher compared to a correct lick (Wilcoxon two-sided rank sum test, $Z = -18.88, p = 1.61 \times 10^{-79}$). (d) PSTH of all tone cells, separated by the distinct lick types as described in Fig. 3i,j. Neurons are sorted by their latency in the TONE choice trials and the sorting is maintained. To specifically examine the response to rewards, only tone cells firing around the target frequency 18–22 kHz have been included. (e) *Left*, PSTH of tone cells around the chosen lick for all incorrect trials. *Middle*, PSTH of the same cells for subsequent exploratory samples after the incorrect lick. Sorting is performed as in (d). *Right*, the average firing rate of the cells for incorrect licks was higher than that for exploratory licks, suggesting some modulation by expectation of the outcome ($n = 633$ reward-related tone cells, Wilcoxon two-sided signed rank test, $z = 6.8, p = 1.03 \times 10^{-11}$). (f) PSTH of tone cells, separated by choice licks at Ports 1–6.

Sorting is performed as in (d). Earlier ports showed a more robust response. Also see Fig. 3m. (g) Average PSTH of reward-related tone cells for choice licks during TONE trials, separated by port numbers (*rainbow colors*). Later (i.e., higher probability) ports had lower firing rate modulation. Statistical comparison is between the average firing rate of the cells within ± 0.3 s around the lick ($n = 633$ cells from 6 mice, Friedman test followed by Tukey-Kramer two-sided post-hoc tests, Chi-sq (5, 3160) = $77.96, p = 2.24 \times 10^{-15}$). Post-hoc comparisons are shown on the *right*. Y axis is on a log scale. (h) Rate maps of all place cells during TONE trial port 6 return runs, shown for NT and TONE trials and separated by correct and incorrect trials. Cells are sorted by TONE correct trials. During incorrect trials, mice did not receive a water reward at the home port. Yet, the firing patterns remained the same. (i) Histogram showing the proportion of place fields at different positions on the track for the return runs. No difference was observed between incorrect and correct trials, even at the home port end of the track. (j, k) Two examples of CA1 tone cells. *Left*, Spatial map and PSTH of the cell for the first lick detected for each port. *Right*, Running speed versus binned firing rate for each cell, plotted as a probability distribution heatmap. Red line, mean firing rate by different speed. The correlation values for both cells were low (Pearson correlation, Cell 1, $R = 0.0712, p = 3.94 \times 10^{-17}$; Cell 2, $R = 0.1055, p = 6.54 \times 10^{-22}$). (l) Distribution of the correlation coefficient of speed and instantaneous firing rate for spatial (black) and tone cells (pink). The two populations were completely overlapping, indicating no preferential speed correlation with either cell “type” ($n = 1129$ tone cells and 1085 neurons with place fields from 6 mice, Wilcoxon two-sided rank sum test, $z = -1.14, p = 0.2531$. ns, not significant) *** $p < 0.001$. Line plots show mean \pm sem.

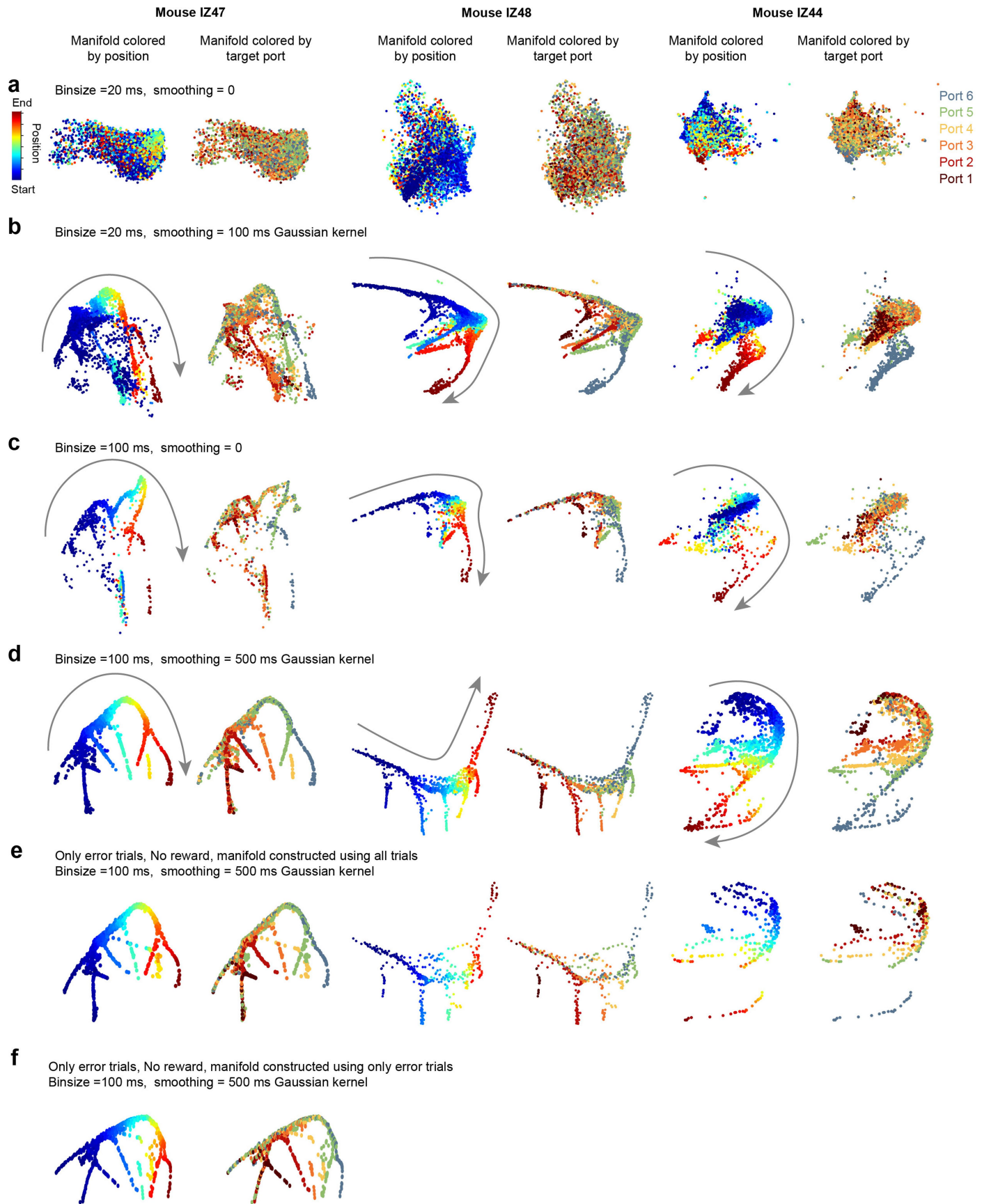


Extended Data Fig. 10 | See next page for caption.

Article

Extended Data Fig. 10 | Firing rate maps do not change or overrepresent a new reward. (a) Example section of the trajectory of the mouse (gray) to highlight behavioral differences after the change in reward condition. Mice often ran incomplete trajectories (highlighted by *red line*) till the unrewarded port in the 1-port condition but ran complete trajectories in the 2-port condition. (b) Trial block correlation for two example CA1 pyramidal cells. The *black line* indicates that the condition change happened between the 5th and the 6th trial blocks. (c) Distribution of place field peak locations (as in Fig. 3e,f) as the mice were running toward the changing reward port (*left*, n = 115 place cells) or when running away from the changing reward port (*right*, n = 146 place cells). Overrepresentation around the ports was observed for both the 1-port and 2-port conditions. (d) Average cell-by-cell correlation between blocks 3-4, blocks 5-6 and blocks 7-8 for all place cells (see Fig. 3g) highlights no significant change in the spatial map upon introduction of the reward (Friedman test followed by Tukey-Kramer two-sided post hoc tests, *Top* (to variable reward), n = 115 cells, Chi-sq (2, 222) = 9.16, p = 0.01; *Bottom* (from variable reward), n = 146 cells, Chi-sq (2, 286) = 1.85, p = 0.397). Significant post-hoc effect shows an increase in stability from blocks 3-4 and 7-8, and is not related to blocks 5-6, which is where the reward is introduced. (e) Schematic highlighting the selection criterion for neurons whose place field center was within 20 cm

of the changing reward port. (f) Average cell-by-cell trial block correlation for neurons selected according to (e). *Black line* indicates that the condition change happened between the 5th and the 6th trial blocks. Black circles, selected trial block comparisons shown in (g). (g) Average cell-by-cell correlation between blocks 3-4, blocks 5-6 and blocks 7-8 for each running direction (Friedman test followed by Tukey-Kramer two-sided post-hoc tests, *top*; n = 39 place cells, Chi-sq (2, 37) = 2.00, p = 0.3679, *bottom*; n = 61 place cells, Chi-sq (2, 61) = 3.18, p = 0.2039). (h) Schematic highlighting the selection criterion for neurons whose place field center was within 20 cm of the stable reward port. The mouse schematics in panels e,h were created using SciDraw (<https://scidraw.io>) under a Creative Commons licence CC BY 4.0 (credit E. Tyler and L. Kravitz)⁵¹. (i) Same as (f), but for cells selected according to the criterion in (h). (j) Same as in (g), but for neurons selected according to (h) (Friedman test followed by Tukey-Kramer two-sided post-hoc tests, *top*; n = 45 place cells, Chi-sq (2, 45) = 10.00, p = 0.0067, *bottom*; n = 25 place cells, Chi-sq (2, 24) = 0.0833, p = 0.9592). Significant post-hoc effect shows an increase in stability from blocks 3-4 and 7-8, and is not related to blocks 5-6, which is where the reward is introduced. *p < 0.05, **p < 0.01. All box plots show median ± interquartile; whiskers show range excluding outliers.



Extended Data Fig. 11 | See next page for caption.

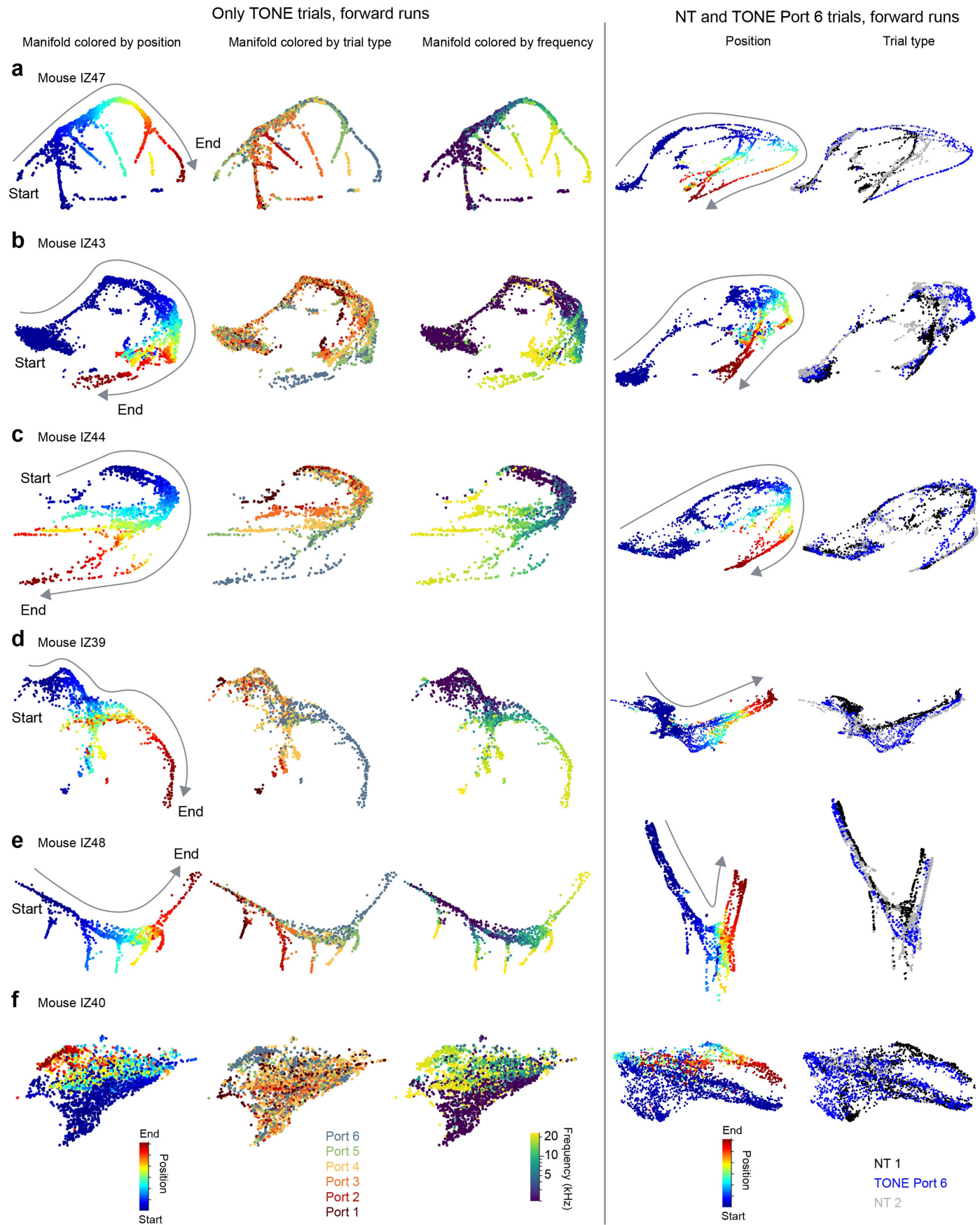
Article

Extended Data Fig. 11 | Effect of binning, smoothing and of rewards on the neural manifold. Neural manifold from three example sessions from separate mice – IZ47 (columns 1,2), IZ48 (columns 3,4) and IZ44 (columns 5,6). The activity of all neurons was binned into time bins of varying duration and various levels of smoothing and visualized on a lower dimension using UMAP. Each dot corresponds to a single time bin colored according to behavior variables. Only the forward running direction during correct TONE trials has been plotted.

Left, Neural manifold colored by the spatial position of the mouse on the track.

Right, Same manifold colored by the target port for that trial. Only times until the first detected lick on a trial are included. (a) Spikes were binned into 20 ms time bins and no smoothing was done. No consistent shape emerged for any of the sessions. (b) Spikes were binned into 20 ms time bins and smoothed using a

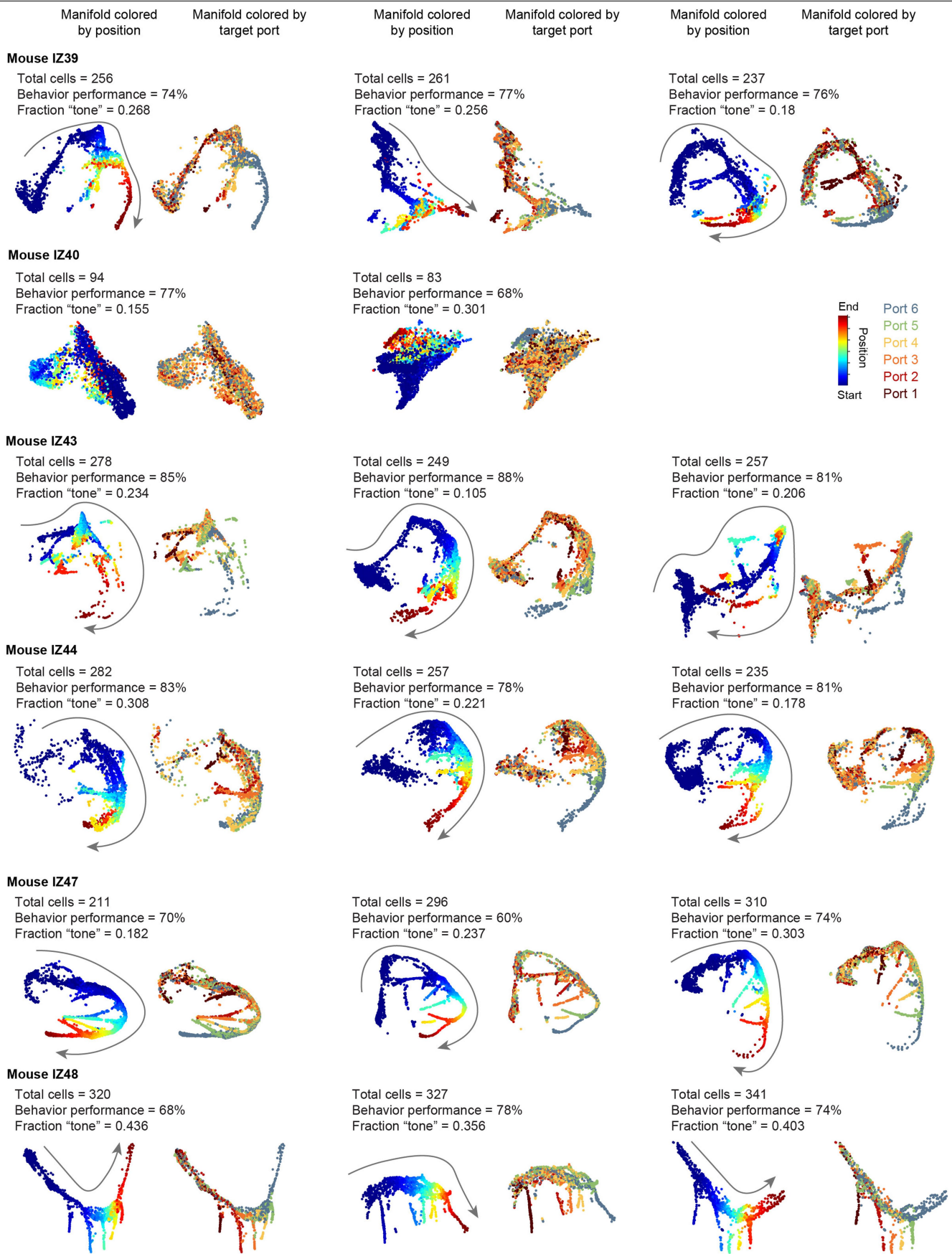
5 bin (100 ms) Gaussian kernel. (c) Spikes were binned into 100 ms time bins and no smoothing was performed. (d) Spikes were binned into 100 ms time bins and smoothed using a 5 bin (500 ms) Gaussian kernel. This condition resulted in the most consistent manifold shape across sessions, but branches were observed with lower binning and smoothing as well. (e) Same as (d) but showing only error trials. The manifold was constructed using the entire session. The manifold shape is conserved between correct and error trials, suggesting that the reward has no major role in the branching. (f) Neural manifold constructed from the session from IZ47, but only using error trials. No reward was ever delivered during these trials, yet the manifold looks almost identical to the one constructed using all trials.



Article

Extended Data Fig. 12 | Distinct branches in the neural manifold were observed across several mice. (a-f) Neural manifolds from example sessions from six mice. Legend and color coding are shown in (f). *First, second and third columns.* Neural manifold that only shows the forward direction runs during correct TONE trials. *First column*, dots of the manifold are colored by spatial position. *Second column*, dots of the manifold are colored by the target port for that trial. Note that the manifold for each mouse had a similar shape with activity evolving along a common trajectory before diverging into distinct branches before the mouse chose a port. *Third column*, dots of the manifold are colored by the tone's frequency. The divergence points occur roughly at

around 10 kHz. *Fourth and fifth columns.* Neural manifold that only shows the forward direction runs during NT and TONE port 6 trials. *Fourth column*, dots of the manifold colored by spatial position. *Fifth column*, dots of the manifold colored by NT1, TONE Port 6, and NT2 trials. Neural trajectories differed depending on trial type – often resulting in more similar trajectories for Port 6 TONE and NT2 trials. Note that mouse IZ40 did not generate a neural manifold with any obvious structure, perhaps because of too few simultaneously recorded neurons (108 cells). See Extended Data Fig. 13 for additional sessions and details.

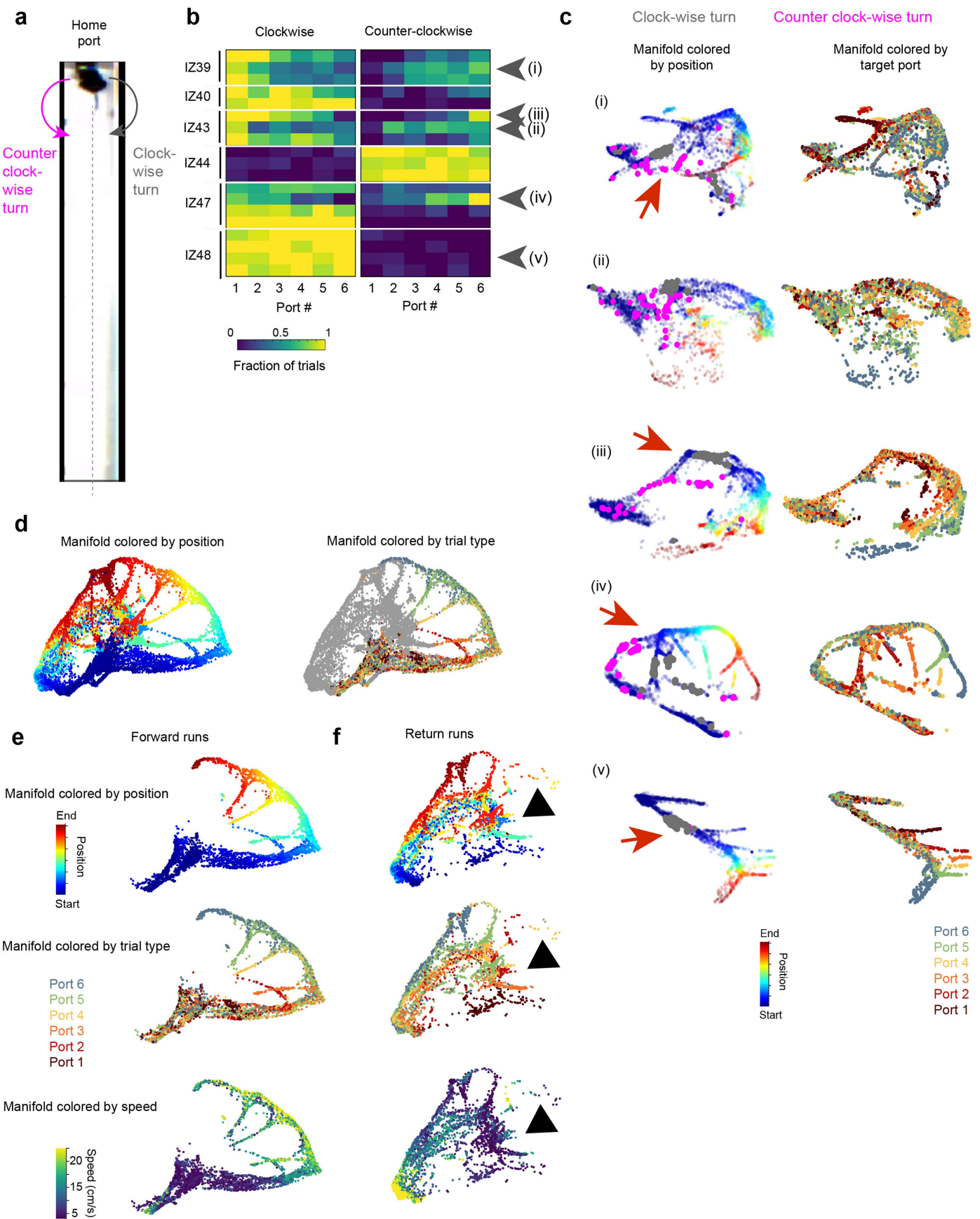


Extended Data Fig. 13 | See next page for caption.

Article

Extended Data Fig. 13 | Variability in the neural manifold across sessions and animals. UMAP displays of 2 or 3 different sessions (*columns*) from each animal (*rows*). Only forward runs of correct TONE trials have been shown. *Left*, manifold colored by spatial position. *Right*, manifold colored by chosen port. The total number of recorded cells, behavior performance and fraction of tone

cells are indicated for each session. While the number of cells was important to establish a general structure of the UMAP display (e.g., IZ 40), it did not appear to explain the precise shape of the UMAP. There was remarkable consistency across sessions within the same animal, yet similar features were also preserved across animals. Arrows show the direction from the start to the end of the track.

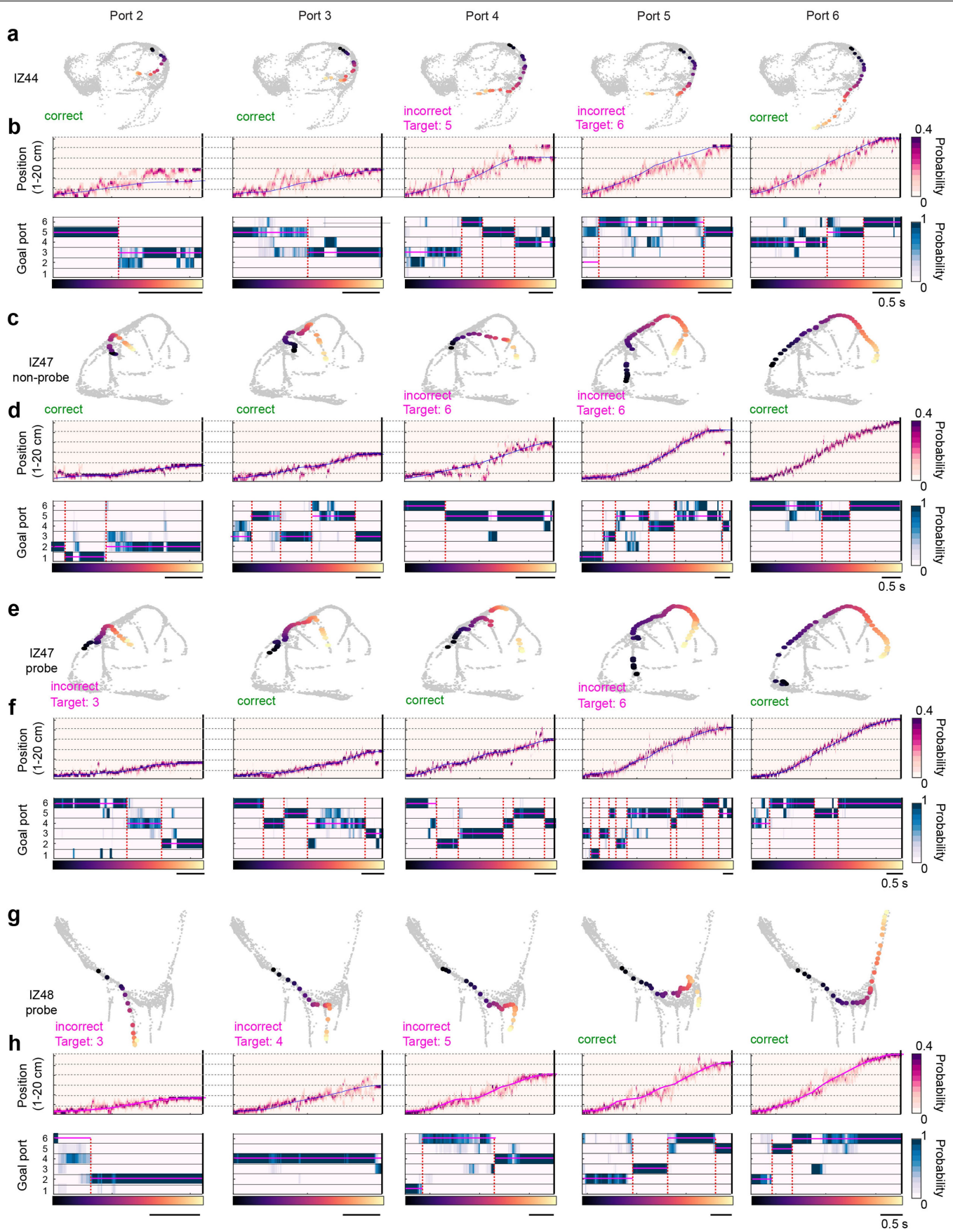


Extended Data Fig. 14 | See next page for caption.

Article

Extended Data Fig. 14 | Direction of rotation and movement of the animal is reflected in the neural manifold. (a) Top view schematic of the mouse licking at the home port. To start the next trial, the mouse can turn clockwise (gray) or counter-clockwise (pink). (b) Fraction of clockwise versus counter-clockwise turns by session (*rows*) and animals (*blocks*). Some mice strongly preferred a single direction (e.g. gray arrowhead in v). In contrast, others showed a target port-dependent relationship in their preference to turn one direction or another (e.g., gray arrowheads i-iv). (c) Neural manifold colored by position and chosen lick port for the sessions marked by gray arrows i-v in (b). The manifold was rotated to optimize the view of the splitting branches (*red arrow*) for clockwise and counter-clockwise turns (*Gray dots*, time of clock-wise turns, *Pink*

dots, counter clock-wise turns). (d) Complete neural manifold of the same session as Fig. 4f, including both forward and return runs, oriented to view both forward and return sections optimally. *Left*, manifold colored by position, *right*, manifold colored by trial type. Return timepoints are shown in gray. Colormap as in (e). (e) Time points corresponding to the forward run from (d). Branches segregate earlier in the trials, before the lick. (f) Time points corresponding to the return run from (d). While branches corresponding to distinct ports were transiently observed (*black arrowhead*), these correspond to moments of low speed (<5 cm/s) continued from the forward run when the mouse is consuming the reward. Once the mouse turns around to start the return run, these branches merge to form a single return run branch.

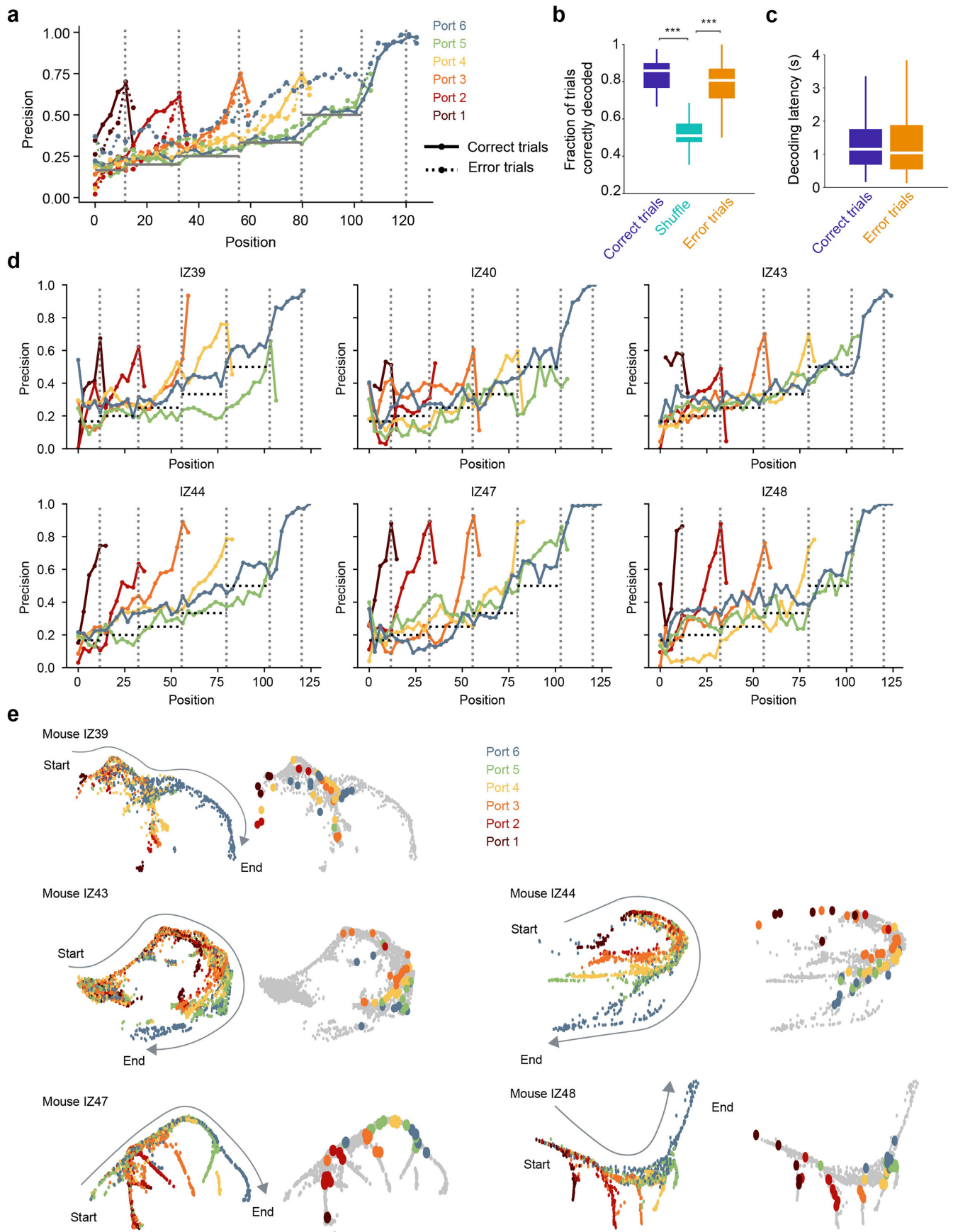


Extended Data Fig. 15 | See next page for caption.

Article

Extended Data Fig. 15 | Examples of single trial UMAP displays, position and goal decoding across mice. (a) *Top*, UMAP (gray dots) of all forward TONE trials from a session by mouse IZ44, overlaid with 5 different single trials going to target ports 2–6 (columns) (colors correspond to time in a trial; colormap shown as x-axis in b). (b) 2-D spatial position and goal decoding (see Methods) using 10 ms time bins. *Top*, Position decoding for the same trials as in (a). *Horizontal dashed lines*, port locations 1–6. *Blue line*, position of the animal. *Bottom*, goal decoding for the same trials as in (a). *Vertical black line* indicates

the time of lick for that trial. *Vertical dashed red line* indicates significant change points (see Methods) when the goal decoding switches. *Pink horizontal lines* show the mode goal decoded between two change points. (c, d) Same as (a,b) but for non-probe trials from a session by mouse IZ47. (e, f) Same as (c,d), but for 4 kHz probe trials from the same session. The trajectory along the neural manifold, goal, and position decoding evolves similarly to the non-probe trials. (g, h) Probe trials from a session from mouse IZ48 (same animal but different session as that of Fig. 4b).



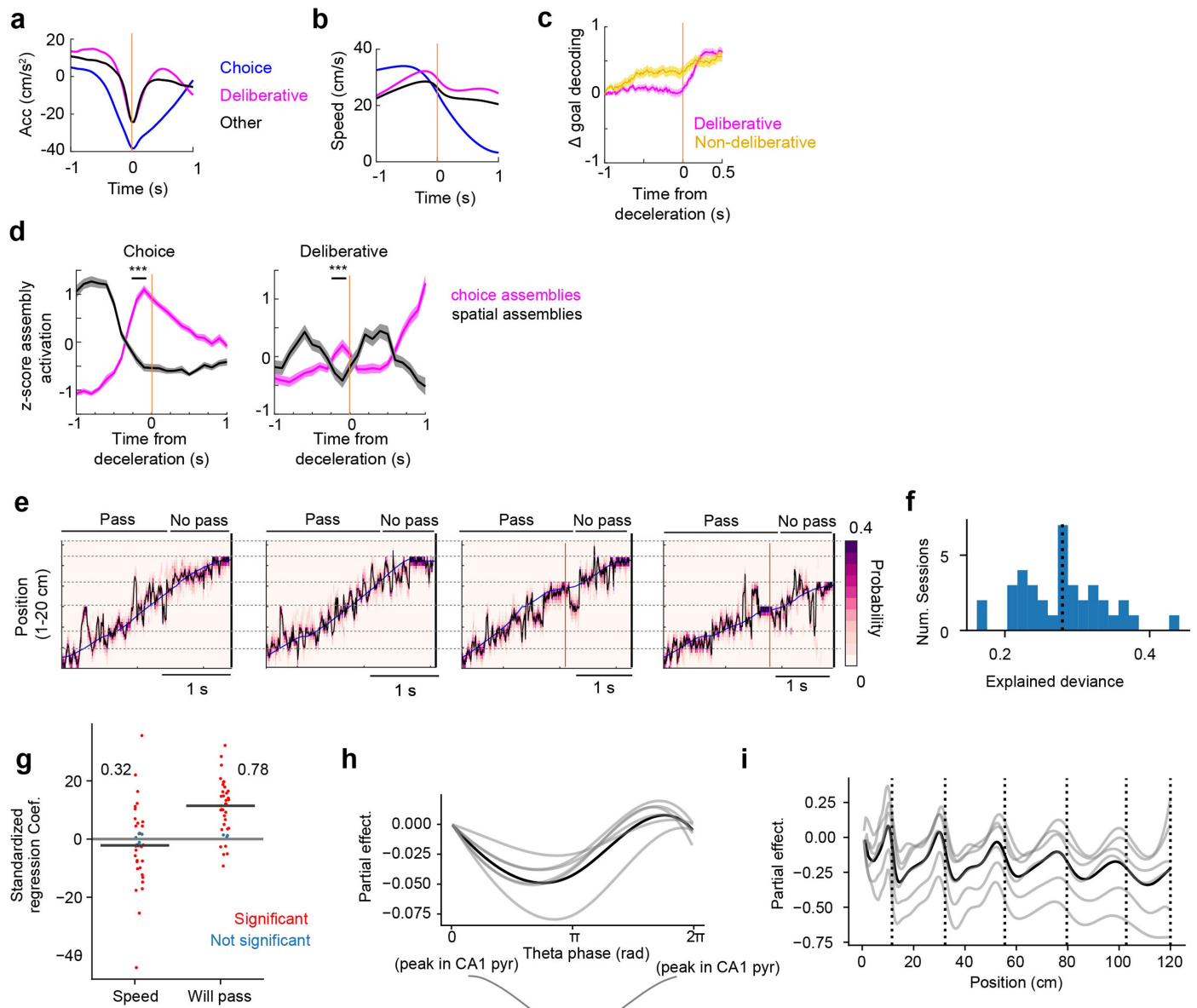
Extended Data Fig. 16 | See next page for caption.

Article

Extended Data Fig. 16 | The target goal can be predicted from population activity.

(a) Decoding of goal ports 1–6 (*colors red to blue*) from population spiking activity as a function of position. The decoder predicted the target port (*vertical gray dashed lines*) on both correct (solid lines) and error (dashed lines) trials above chance (*horizontal solid gray lines*) before the mouse reached the chosen port (37 sessions in 6 mice). (b) Using the change-point method (see Methods), the final prediction of the decoded goal was estimated in every trial and compared to mouse's choice. Note that both correct and error trials had high goal-decoding accuracy compared to a shuffle. In shuffle control the "choice" was randomly selected to be any of the remaining upcoming ports ($n = 37$ sessions from 6 mice, Friedman test followed by Tukey-Kramer two-sided post-hoc tests, Chi-sq (2,72) = 42.98, $p = 4.65 \times 10^{-10}$). (c) The time between the last change point in the decoder and the mouse's choice of the upcoming

port in correct and error trials, i.e., how much before the lick the target port could be predicted (-1.1 s; $n = 1644$, 519 trials, Wilcoxon two-sided rank sum test, $z = 0.9$, $p = 0.3676$). (d) Same as (a), but for individual animals (correct trials only). Mouse IZ40 with few cells had a poor decoding performance. *Horizontal dashed black lines* indicate chance levels. (e) Example neural manifold of each animal (except IZ40). All time points from forward TONE trials are shown. *Left*, dots colored by the target port. *Right*, all dots are shown in gray. Superimposed dots correspond to the time of the final detected change point during correct trials. *Colors* indicate trials corresponding to ports 1–6. Decoding for each trial fell on the branch points for each target on the manifold, more clearly visible when the manifold branches were farther apart. Also see Fig. 4f,g. *** $p < 0.001$. All box plots show median \pm interquartile; whiskers show range excluding outliers.



Extended Data Fig. 17 | See next page for caption.

Article

Extended Data Fig. 17 | Relationship between speed deceleration and theta look-ahead within a trial. (a) All significant decelerations during forward TONE trials were separated into three categories – choice (approaching target port; *blue*), deliberative (slowing down near a non-target port, without licking; *pink*), and “other” (all other detected decelerations; *black*). Deliberative and other decelerations had similar acceleration profiles. Choice decelerations had more pronounced troughs. All sessions across all mice. Standard error is too small to be observable. (b) Same as (a) but showing the speed profile. Despite a significant deceleration, the speed of the mouse remained high during deliberative and other decelerations. (c) The change in goal decoding from the neuronal population against deliberative decelerations (*pink*, also shown in Fig. 5g). *Yellow*, as a control, extracted from random times when the mouse was crossing a port but did not decelerate (equal number of time points as in deliberative decelerations). Thus, the jump in the decoder does not occur because of specific port cues. Lines show mean \pm sem. (d) The expression of cell assemblies as defined in Fig. 2c–e was examined during decelerations. Choice assemblies (*pink*) were defined as assemblies with a peak activation in the 300 ms window preceding a lick, while spatial assemblies (*black*) had a peak activation from 1 s to 700 ms preceding a lick (*left*). During deliberative decelerations (*right*), choice assemblies transiently increased their expression while spatial assemblies decreased their expression, indicating assembly flickering ($n = 90$ choice assemblies and 59 spatial, activation at 200 ms before the deceleration, Wilcoxon rank-sum two-sided test, Choice, $p = 5.89 \times 10^{-13}$. Deliberation, $p = 1.62 \times 10^{-4}$). Lines show mean \pm sem. (e) Four example trials show position decoding from neuronal population within a trial. The likelihood of decoding a jump beyond the next port is higher if the mouse passes versus if the mouse licks at the port (not pass). Examples 3 and 4 show brief narrowing of the decoding before deliberation (*yellow vertical line*). Smooth blue line, true position, black line, decoded mouse position. (f) A generalized additive model (GAM; see Experimental Procedures) was fit to predict the summed posterior beyond the upcoming port, using the linear regressors *speed* and *will_pass* (whether the animal will pass the upcoming port) and smooth function (via B-spline basis functions) regressors *theta phase* and *position*. Blue bars show the distribution of the model’s explained deviance in all sessions. The vertical dotted line marks the mean. (g) Standardized regression coefficients (per session) for the linear terms: *Speed* and *Will_pass*, to predict whether the position decoding posterior is beyond the upcoming port. Color marks whether the coefficient is significant based on the asymptotic standard errors based on the Fisher information matrix. Numbers refer to the fraction of sessions with positive and significant regression coefficients. This plot shows that the running speed did not impact the position decoding posterior, which instead was strongly dependent on whether the mouse would run past the port. (h) The partial effect of theta-phase of the summed posterior after the upcoming port. Each grey line is the average over sessions within an animal. Black line, group average over all sessions. The grey line on the bottom is the LFP theta cycle. We observe an increase in the partial effect in the ascending phase of theta. Thus, there is a greater “lookahead” (i.e., probability of the position decoding posterior to be beyond the upcoming port), specifically during the ascending phase of theta. (i) Similar to (h), but with the partial effect of *position*. The vertical dotted lines mark the positions of the ports. The partial effect ramps up towards the port and falls after the port by design because the predicted variable is the summed posterior beyond the next port. This position value is only included as a control to confirm that the GAM fit is reasonable. It does not show more theta lookahead (relative to the animal) as the mouse approaches the port.

Reporting Summary

Nature Portfolio wishes to improve the reproducibility of the work that we publish. This form provides structure for consistency and transparency in reporting. For further information on Nature Portfolio policies, see our [Editorial Policies](#) and the [Editorial Policy Checklist](#).

Statistics

For all statistical analyses, confirm that the following items are present in the figure legend, table legend, main text, or Methods section.

n/a Confirmed

- The exact sample size (n) for each experimental group/condition, given as a discrete number and unit of measurement
- A statement on whether measurements were taken from distinct samples or whether the same sample was measured repeatedly
- The statistical test(s) used AND whether they are one- or two-sided
Only common tests should be described solely by name; describe more complex techniques in the Methods section.
- A description of all covariates tested
- A description of any assumptions or corrections, such as tests of normality and adjustment for multiple comparisons
- A full description of the statistical parameters including central tendency (e.g. means) or other basic estimates (e.g. regression coefficient) AND variation (e.g. standard deviation) or associated estimates of uncertainty (e.g. confidence intervals)
- For null hypothesis testing, the test statistic (e.g. F , t , r) with confidence intervals, effect sizes, degrees of freedom and P value noted
Give P values as exact values whenever suitable.
- For Bayesian analysis, information on the choice of priors and Markov chain Monte Carlo settings
- For hierarchical and complex designs, identification of the appropriate level for tests and full reporting of outcomes
- Estimates of effect sizes (e.g. Cohen's d , Pearson's r), indicating how they were calculated

Our web collection on [statistics for biologists](#) contains articles on many of the points above.

Software and code

Policy information about [availability of computer code](#)

Data collection	Commercially available software from Intan RHX (version 3.3.2) was used for data collection. Arduino IDE 2.0 was used to interface the behavior apparatus. Bonsai 2.8.5 was used for real-time detection of the mouse position.
Data analysis	MATLAB R2023b was used for data analysis. All custom code for preprocessing the data is freely available on the Buzsaki Lab repository: https://github.com/buzsakilab/buzcode . Code for the P-GAM implantation is freely available on https://github.com/BalzaniEdoardo/PGAM . Scripts specific to analyzing this dataset are available on I.Zutshi's github page, https://github.com/ipshtitaZutshi/JungleBook/tree/main/ToneTask .

For manuscripts utilizing custom algorithms or software that are central to the research but not yet described in published literature, software must be made available to editors and reviewers. We strongly encourage code deposition in a community repository (e.g. GitHub). See the Nature Portfolio [guidelines for submitting code & software](#) for further information.

Data

Policy information about [availability of data](#)

All manuscripts must include a [data availability statement](#). This statement should provide the following information, where applicable:

- Accession codes, unique identifiers, or web links for publicly available datasets
- A description of any restrictions on data availability
- For clinical datasets or third party data, please ensure that the statement adheres to our [policy](#)

The dataset generated for this study has been made publicly available in the Buzsaki lab repository: <https://buzsakilab.nyumc.org/datasets/Zutshil/Nature2024/>

Research involving human participants, their data, or biological material

Policy information about studies with [human participants or human data](#). See also policy information about [sex, gender \(identity/presentation\), and sexual orientation](#) and [race, ethnicity and racism](#).

Reporting on sex and gender

N/A

Reporting on race, ethnicity, or other socially relevant groupings

N/A

Population characteristics

N/A

Recruitment

N/A

Ethics oversight

N/A

Note that full information on the approval of the study protocol must also be provided in the manuscript.

Field-specific reporting

Please select the one below that is the best fit for your research. If you are not sure, read the appropriate sections before making your selection.

Life sciences

Behavioural & social sciences

Ecological, evolutionary & environmental sciences

For a reference copy of the document with all sections, see nature.com/documents/nr-reporting-summary-flat.pdf

Life sciences study design

All studies must disclose on these points even when the disclosure is negative.

Sample size

Animals from the control paradigm and auditory task paradigm were run in parallel cohorts. No specific analysis was used to estimate minimal population sample, but the number of animals, trials and recorded cells were larger than or similar to those employed in previous studies (McKenzie et al., 2021; Senzai et al., 2019; Valero et al., 2021; Zhang et al., 2021).

Data exclusions

No data were excluded from the analysis

Replication

Data from animals was collected in four separate cohorts, and the results were consistent across animal cohorts and strains.

Randomization

Animals were randomly allocated to be trained for the control version of the task.

Blinding

Blinding was not relevant to the study. Different groups of animals were trained on control and task versions of the task, making blinding irrelevant

Reporting for specific materials, systems and methods

We require information from authors about some types of materials, experimental systems and methods used in many studies. Here, indicate whether each material, system or method listed is relevant to your study. If you are not sure if a list item applies to your research, read the appropriate section before selecting a response.

Materials & experimental systems

n/a	Involved in the study
<input checked="" type="checkbox"/>	Antibodies
<input checked="" type="checkbox"/>	Eukaryotic cell lines
<input checked="" type="checkbox"/>	Palaeontology and archaeology
<input type="checkbox"/>	Animals and other organisms
<input checked="" type="checkbox"/>	Clinical data
<input checked="" type="checkbox"/>	Dual use research of concern
<input checked="" type="checkbox"/>	Plants

Methods

n/a	Involved in the study
<input checked="" type="checkbox"/>	ChIP-seq
<input checked="" type="checkbox"/>	Flow cytometry
<input checked="" type="checkbox"/>	MRI-based neuroimaging

Animals and other research organisms

Policy information about [studies involving animals; ARRIVE guidelines](#) recommended for reporting animal research, and [Sex and Gender in Research](#)

Laboratory animals

We used a combination of transgenic and wildtype male mice [Auditory task; n = 6 male mice of which 4 were double transgenic mice crossed between Pvalb- IRES-Cre females (Jax Stock No. 017320) and Ai32 males (Jax Stock No. 024109). The other 2 mice were C57BL/6J wildtypes (Jax Stock No. 000664). At the time of implantation, mice ranged from 3-6 months of age and 22-31g in weight. Mice were housed at around 22°C, with a relative humidity of around 45%.

Wild animals

This study did not involve wild animals

Reporting on sex

Only male mice were used due to their heavier weights, which allows them to more easily carry the implants in the freely moving task.

Field-collected samples

This study does not include field-collected samples

Ethics oversight

All experiments were approved by the Institutional Animal Care and Use Committee at New York University Langone Medical Center.

Note that full information on the approval of the study protocol must also be provided in the manuscript.

Plants

Seed stocks

Report on the source of all seed stocks or other plant material used. If applicable, state the seed stock centre and catalogue number. If plant specimens were collected from the field, describe the collection location, date and sampling procedures.

Novel plant genotypes

Describe the methods by which all novel plant genotypes were produced. This includes those generated by transgenic approaches, gene editing, chemical/radiation-based mutagenesis and hybridization. For transgenic lines, describe the transformation method, the number of independent lines analyzed and the generation upon which experiments were performed. For gene-edited lines, describe the editor used, the endogenous sequence targeted for editing, the targeting guide RNA sequence (if applicable) and how the editor was applied.

Authentication

Describe any authentication procedures for each seed stock used or novel genotype generated. Describe any experiments used to assess the effect of a mutation and, where applicable, how potential secondary effects (e.g. second site T-DNA insertions, mosaicism, off-target gene editing) were examined.